Interplay of magnetic field and interlayer coupling in the quasi-two-dimensional quantum magnet $Cu(en)Cl_2$: Realization of the spin-1/2 rectangular/zigzag square Heisenberg lattice

L. Lederová,[1] A. Orendáčová,[1,*] R. Tarasenko,[1] K. Karl'ová,[1] J. Strečka,[1] A. Gendiar,[2] M. Orendáč,[1] and A. Feher[1]

[1]*Institute of Physics, P.J. Šafárik University, Park Angelinum 9, 040 00 Košice, Slovakia*

[2]*Institute of Physics, Slovak Academy of Sciences, SK-845 11 Bratislava, Slovakia*

(Received 11 July 2019; published 11 October 2019)

The interplay of the magnetic field and interlayer correlations was experimentally investigated in a quasi-two-dimensional quantum magnet $Cu(en)Cl_2$. For this purpose, extensive quantum Monte Carlo (QMC) studies of the finite-temperature properties of the spin-1/2 Heisenberg antiferromagnet (HAF) on the rectangular and the spatially anisotropic zig-zag square lattices were performed. The QMC studies revealed the equivalency of both models for any values of magnetic fields and spatial anisotropies $R = J_{\text{interchain}}/J_{\text{intrachain}}$. The analysis based on the decomposition of both lattices into local Hamiltonians confirmed the equivalence. Despite the large influence of the interlayer coupling and rather complicated distribution of the intralayer exchange pathways in $Cu(en)Cl_2$, considering several constraints in the data analysis enabled the extraction of the main features of the low-dimensional magnetic subsystem from the specific heat and magnetization. It was found that $Cu(en)Cl_2$ can be treated as the realization of the spin-1/2 HAF on the rectangular/zig-zag square lattice with the intralayer spatial anisotropy $R \approx 0.2$, the intrachain exchange coupling 2.20 ± 0.15 K, the saturation field 3.7 ± 0.1 T, the spin-flop field about 0.1 T, and the spin anisotropy of the orthorhombic symmetry. The possibility to investigate magnon instabilities in the strong-field regime of $Cu(en)Cl_2$ is discussed.

DOI: 10.1103/PhysRevB.100.134416

I. INTRODUCTION

A Heisenberg antiferromagnet (HAF) on the square lattice with spin 1/2 represents an important paradigm of two-dimensional (2D) magnetism. After long debate a final form of the ground state of the model was established as a collinear Néel order with a partially reduced order parameter (staggered magnetization) due to strong quantum fluctuations [1]. In the rectangular lattice (RL), derived from the square lattice after weakening the exchange coupling in one direction, the strength of the fluctuations increases and, finally, a fully disordered Luttinger liquid ground state can be achieved in the one-dimensional (1D) limit. Despite intensive ground-state theoretical studies, experimental realizations of the spin-1/2 HAF on the rectangular lattice appeared only recently [2,3]. The main problem in the identification of the proper materials was the absence of adequate theoretical predictions. What is more, later theoretical calculations revealed a close similarity of the finite-temperature properties of the 2D spin-1/2 HAF models on the square and the rectangular lattice for some ratios of the intrachain J_1 and the interchain J_2 couplings. As a consequence, the analysis of the experimental data can lead to the oversight of the spatial anisotropy within the magnetic layer [2,3]. Besides the similarity of the finite-temperature properties of these 2D quantum spin models, the interlayer interactions being always present in real materials can modify to some extent the finite-temperature properties.

The inclusion of the nonfrustrated interlayer coupling J' suppresses the quantum fluctuations, which leads to the enhancement of the order parameter in comparison to its 2D counterpart [4]. In addition, the stabilization of the three-dimensional (3D) long-range order (LRO) at a finite temperature T_N appears [5]. Depending on the strength of J', the deviations from the pure 2D correlations can prevent the correct identification of the actual 2D magnetic system forming at temperatures above T_N [4,6]. Quantum Monte Carlo studies of the spin-1/2 HAF on the spatially anisotropic simple cubic (SC) lattice (for $J' = 0$ the SC lattice decomposes into the 3D array of the independent 2D layers with the square-lattice motif and the intralayer nearest-neighbor coupling $J_1 = J_2 = J$) revealed that a sharp λ-like peak in the specific heat associated with the phase transition to 3D LRO completely vanishes for $J' < 0.015J$, and despite the onset of the 3D LRO the specific heat follows the behavior of the 2D system [6]. Such extreme weakness of the interlayer coupling accompanied by the absence of the aforementioned sharp specific-heat anomaly in the zero magnetic field was already experimentally observed in $Cu(tn)Cl_2$ ($tn = C_3H_{10}N_2$) [7] and $Cu(pz)_2(pyO)_2(PF_6)_2$ (pyO = pyridine-N-oxide) [8]. The studies of the polycrystalline $Cu(tn)Cl_2$ identified the compound as a spin-1/2 quasi-2D quantum magnet with the saturation field $B_{sat} \approx 6.5$ T and the effective intralayer exchange coupling $J^{eff}/k_B \approx 3$ K[7].

To find more information on the character of the exchange pathways, we modified the structure of $Cu(tn)Cl_2$ by substituting the organic ligand *tn* by smaller *en* (ethylenediamine $= C_2H_8N_2$). Despite the small difference between the spatial geometry of *tn* and *en* ligands, their mutual substitution proved to have large impact on the crystal symmetry; while the structure of $Cu(tn)Cl_2$ is orthorhombic, its *en* analog crystalizes in the monoclinic space group [9–14]. Besides the

*alzbeta.orendacova@upjs.sk

room-temperature susceptibility and electron paramagnetic resonance experiments [15,16], no other magnetic studies were reported for this compound.

Our recent investigations of magnetostructural correlations [17] revealed that at temperatures above 20 K magnetic susceptibilities of Cu(*tn*)Cl_2 and Cu(*en*)Cl_2 become identical within the experimental inaccuracy. The observed behavior was ascribed to the close similarity of Cu(II) chromophores CuN_2Cl_4 in both compounds. The differences appearing at lower temperatures reflect the influence of magnetic correlations, which grow with a different intensity in each compound.

The present paper is focused on the identification of a 2D magnetic system in Cu(*en*)Cl_2 on the basis of the comparative analysis of the experimental and theoretical specific heat, magnetic entropy, susceptibility, and magnetization data. For this purpose, extensive quantum Monte Carlo studies of the spin-1/2 HAF on the rectangular and spatially anisotropic zig-zag square lattices (ZZLs) were performed in a wide range of magnetic fields and spatial anisotropies. Despite rather strong influence of the interlayer coupling in Cu(*en*)Cl_2, the analysis supported by considering several constraints enabled us to quantify the contribution of LRO and short-range order (SRO) to finite-temperature properties.

This paper is organized as follows. A synthesis procedure, crystal structure, distribution of exchange pathways, and experimental details are described in Sec. II. Section III involves quantum Monte Carlo calculations of finite-temperature properties of the spin-1/2 HAF on the rectangular and spatially anisotropic zig-zag square lattices, performed in a wide range of magnetic fields and spatial anisotropies. Section IV is focused on the analysis of the experimental specific heat, susceptibility, and magnetization data. The possibility of the observation of magnon instability in Cu(*en*)Cl_2 in the strong-field regime is discussed as predicted theoretically for the spin-1/2 HAF on the square lattice in the magnetic fields above some threshold field. The results together with some conclusions are summarized in Sec. V.

II. CRYSTAL STRUCTURE AND EXPERIMENTAL DETAILS

Following the synthesis reported in Ref. [10], single crystals of Cu(*en*)Cl_2 were prepared from the equimolar mixture of $CuCl_2 \cdot H_2O$ and ethylenediamine in the form of dark blue plates. The identity of the compound was verified at room temperature using the infrared spectroscopy and x-ray powder diffraction.

At room temperature, the compound crystallizes in the monoclinic space group $P2_1/m$, with the unit-cell parameters $a \times b \times c = 8.219 \times 5.747 \times 6.776\,\text{Å}^3$, $\beta = 93.72^\circ$, $Z = 2$, $\rho = 2.02\,\text{g cm}^{-3}$. The copper atom is surrounded by two Cl atoms and two N atoms from the ethylenediamine [Fig. 1(a)] in the cis square-planar arrangement [d(Cu-Cl1) = 2.286 Å, d(Cu-Cl2) = 2.301 Å, d(Cu-N1) = 2.010 Å, d(Cu-N2) = 2.017 Å] [10]. The molecules are arranged into chains running parallel to the b axis; the displacement of Cu atoms from the 2_1 axis allows Cl2 atoms to lie directly above and below Cu atoms in adjacent molecules with the separation d(Cu-Cl2 a, b) = 2.887 Å). As a consequence, the structure is composed of infinite ladder-type ribbons running parallel to the b axis in which Cu atoms are coordinated by four Cl and two N ligands forming a distorted octahedron elongated along the ladders [Fig. 1(a)]. The hydrogen bonding along the c axis is responsible for the disorder in the ethylenediamine ring where the carbon atoms can occupy two positions related by a mirror plane m [10,18]. Below a phase transition at about 138 K the structure transforms to the space group $P2_1/c$ with the unit-cell parameters $a \times b \times c = 8.1729 \times 5.7266 \times 13.4626\,\text{Å}^3$, $\beta = 95.076^\circ$, $Z = 4$ [18]. The low-temperature structure is again composed of the ladders, and the geometry of the local surroundings of the Cu atom remains octahedral; however, the carbon disorder has disappeared. Instead of the equal amount of both conformations of the *en* rings on each position reported for the high-temperature phase [10], below the phase transition, the *en* rings with the opposite chirality occupy fixed positions in the chains related to each other by the gliding operation [Fig. 1(b)].

Considering the distorted octahedral surroundings of the Cu atom, the local geometry stabilizes the d_z^2 electronic ground state and, hence, the unpaired electron should be described by the wave function of $d_{x^2-y^2}$ symmetry. Such atomic arrangement should support the formation of exchange pathways along the $d_{x^2-y^2}$ lobes within the equatorial plane of the distorted octahedron formed by N1, N2, Cl1, and Cl2 atoms [Fig. 1(a)]. The inspection of the low-temperature structure revealed several short distances between the equatorial ligands (Cl $\cdots$ Cl, Cl $\cdots$ N) from neighboring Cu atoms. While within the bc plane the distances $d_{\text{Cl-Cl}}$ and $d_{\text{Cl-N}}$ range between 3.3 and 3.8 Å, the corresponding distances along the a axis are much longer, the shortest one exceeding 5 Å.

Thus, assuming formation of exchange pathways along the aforementioned pairs with short separations, a two-dimensional magnetic lattice within the bc plane can be expected in Cu(*en*)Cl_2. The spatial distribution of the potential exchange pathways forms a rectangular lattice with additional interactions along one of the diagonals of the rectangular plaquettes [Figs. 1(c) and 1(d)].

Specific-heat measurements in the magnetic fields $B(=\mu_0 H)$ from 0 to 9 T and temperatures nominally from 0.4 to 15 K were performed using a commercial (Quantum Design Physical Property Measurement System) device equipped with the ^{3}He insert. The specific-heat data were corrected for the addenda contribution, which was measured in a separate run. Magnetization and magnetic susceptibility were measured in the temperature range from 0.5 to 2 K in the fields up to 5 T using a commercial (Quantum Design Magnetic Property Measurement System) device equipped with the ^{3}He insert. The measurements were performed in the field cooling (FC) and zero-field cooling (ZFC) regimes. All magnetic measurements in very small magnetic fields (i.e. in the mT region) were preceded by the magnet-reset option to exclude the effect of frozen magnetic fields in the superconducting coil. In all physical measurements, single crystals from the same batch were used, with the typical dimensions $d_1 \times d_2 \times d_3 \approx 1 \times 4 \times 2\,\text{mm}^3$. The longest edge d_2 is parallel with the b axis, while the shortest d_1 is parallel with the a axis [9,16]. The direction along the medium edge d_3 denoted as c^* coincides with the c axis within a few degrees.

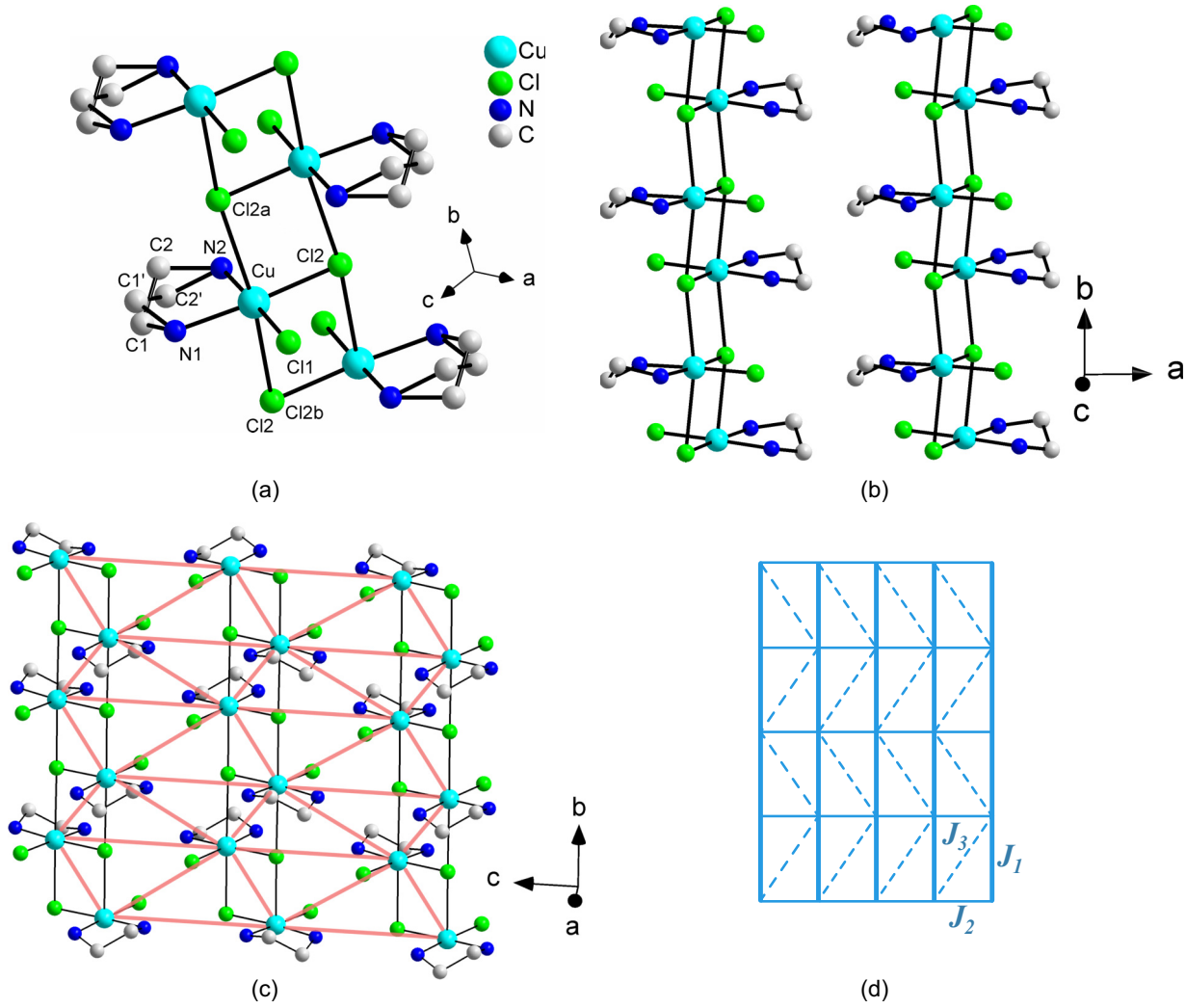

FIG. 1. (a) Fragment of the high-temperature structure of Cu(*en*)Cl_2 demonstrating the octahedral surrounding of the Cu atom. Both conformations of the *en* ring are shown. (b) Projection of the low-temperature structure in the *ab* plane. For clarity, hydrogen atoms and hydrogen bonds are not shown. (c) Distribution of expected exchange pathways within the *bc* plane. (d) Schematic drawing of the corresponding rectangular lattice with the nearest-neighbor J_1 and J_2 couplings and the additional next-nearest-neighbor coupling J_3 along one of the diagonals of the rectangular plaquettes.

III. QUANTUM MONTE CARLO CALCULATIONS

The expected exchange pathways in Fig. 1(c) form a two-dimensional magnetic lattice, which corresponds to the spin-1/2 HAF on the rectangular lattice with the nearest-neighbor couplings J_1 and J_2 and the additional next-nearest-neighbor (NNN) coupling J_3 along one of the diagonals of the rectangular plaquettes [Fig. 2(a)]. Without the exact knowledge of which of the couplings can be considered as the weakest, the full model can be simplified in several ways.

(i) $J_1 = 0$: The lattice transforms to the rectangular lattice with the nearest-neighbor interactions J_2 and J_3.

(ii) $J_3 = 0$: The lattice transforms again to the rectangular lattice with the nearest-neighbor interactions J_1 and J_2.

(iii) $J_2 = 0$: The lattice transforms to the linear chains coupled via zig-zag further-neighbor coupling, which is equivalent to the spatially anisotropic zig-zag square lattice (Fig. 2).

The tuning of the spatial anisotropy of the exchange coupling in the lattices depicted in Figs. 2(b)–2(e) enables their interpolation between the array of the isolated linear chains and the spatially isotropic square lattice. Besides the ground-state properties, finite-temperature properties of both limiting lattice models have been investigated in detail for zero and nonzero magnetic field [19–23].

Concerning the lattices in Figs. 2(b)–2(e), there is a lack of proper theoretical predictions for the finite-temperature behavior. For the spin-1/2 HAF on the rectangular lattice in zero magnetic field, temperature dependence of the correlation length, uniform susceptibility, magnetization, and specific heat has been evaluated by means of quantum Monte Carlo (QMC) simulations [3,24–26] for some values of the spatial anisotropies $R = J_{\text{interchain}}/J_{\text{intrachain}}$ ranging between 0 and 1. More systematic theoretical studies of finite-temperature properties are available for the spin-1/2 HAF on the spatially anisotropic zig-zag square lattice [27,28].

It should be noted that besides the chain ($R = 0$) and isotropic square lattice ($R = 1$) the finite-temperature theoretical studies of the spin-1/2 HAF on the rectangular and zig-zag

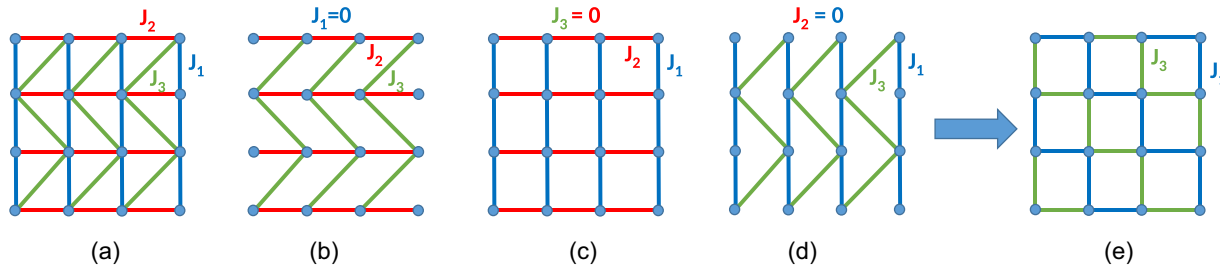

FIG. 2. (a) Rectangular lattice with the nearest-neighbor couplings J_1 and J_2 and the additional next-nearest-neighbor coupling J_3 along one of the diagonals of the rectangular plaquettes. (b), (c) Rectangular lattices derived from (a). The lattice denoted by (d) is topologically equivalent to the spatially anisotropic zig-zag square lattice (e). In the Hamiltonian (1) (see text below), J_1 and J_3 in (e) correspond to J and RJ, respectively.

lattice in the external magnetic field are missing. Owing to this fact, a comprehensive analysis of the basic response functions usually measured in the experiment was performed in the present paper.

A. Spin-1/2 HAF on the spatially anisotropic zig-zag square lattice

The model of the spin-1/2 HAF on the spatially anisotropic zig-zag square lattice [Fig. 2(e)] in the magnetic field is described by the Hamiltonian [27]

$$H = J\left[\sum_{i,j} \mathrm{S}_i\mathrm{S}_j + R\sum_{k,l} \mathrm{S}_k\mathrm{S}_l\right] - g\mu_B B\sum_{i=1}^{N} S_i^z, \qquad (1)$$

where the parameter $J > 0$ stands for the Heisenberg antiferromagnetic exchange coupling $J_{\mathrm{intrachain}}$, JR represents $J_{\mathrm{interchain}}$, and the anisotropy parameter R ranges from 0 to 1. The first and second summations involve the interaction

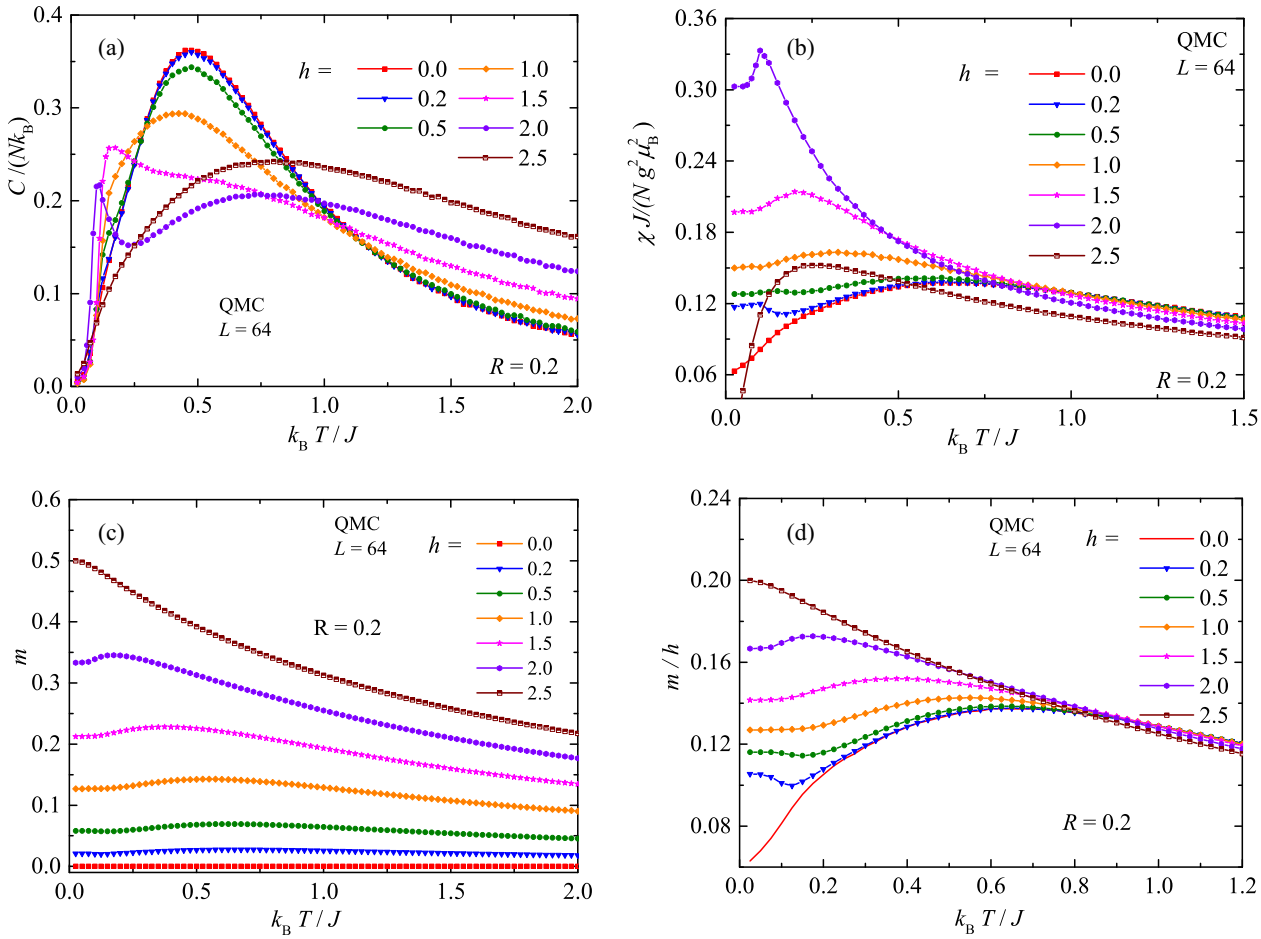

FIG. 3. (a) Temperature dependence of the specific heat of the spin-1/2 HAF on the spatially anisotropic zig-zag square lattice [Eq. (1)] with $R = 0.2$ and $L = 64$ in constant magnetic fields. Temperature dependence of (b) the reduced susceptibility, (c) the reduced magnetization, and (d) the *m/h* ratio, calculated for the aforementioned model. For clarity, in the high field $h = 3.5$, only specific heat is shown.

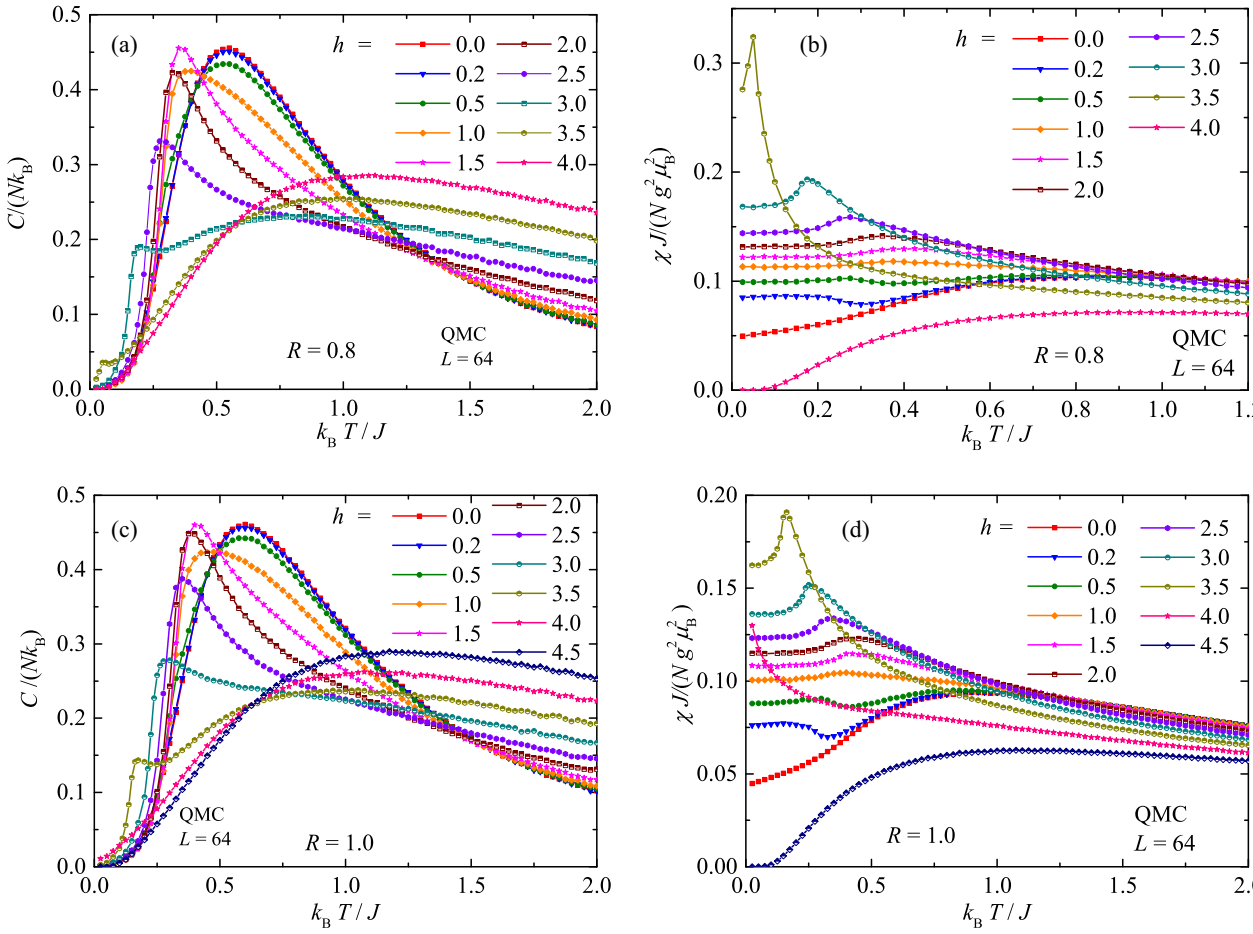

FIG. 4. Temperature dependence of the specific heat and susceptibility of the spin-1/2 HAF on the spatially anisotropic zig-zag square lattice ($L = 64$) in constant magnetic field [Eq. (1)] with $R = 0.8$ (a), (b) and $R = 1$ (c), (d).

between nearest neighbors within the same zig-zag chain and between the nearest neighbors from different zig-zag chains, respectively. The last term in Eq. (1) is the usual Zeeman term (g is the Landé factor; μ_B is the Bohr magneton).

Following the procedures developed in Ref. [27], all calculations were conducted using a directed loop algorithm in the stochastic series expansion representation of the quantum Monte Carlo method [29] from Algorithms and Libraries for Physics Simulations project [30]. The QMC simulations were performed on finite-size lattices with a linear size L, which involve under the periodic boundary conditions in total $N = 4L \times L$ spins. The comparative studies with $L = 32$ and 64 found no finite-size effects. The adequate numerical accuracy was achieved through 8×10^5 Monte Carlo steps used for a statistical averaging in addition to 1.5×10^5 steps for thermalization.

The calculations of thermodynamic quantities were performed for $R = 0.1$, 0.2, 0.4, 0.6, 0.8, and 1. For each R, temperature dependences of the specific heat C, susceptibility χ, and uniform magnetization $m = M/(Ng\mu_B)$ were calculated in the constant magnetic field $h = g\mu_B B/J$, nominally ranging from 0 to 5. (The value $h = 4$ corresponds to the saturation field of the isotropic square lattice.) Temperature dependences of the thermodynamic quantities for $R = 0.2$, 0.8, and 1 in various magnetic fields are depicted in Figs. 3 and 4.

The specific heat of the model [Eq. (1)] has a few characteristic features, which persist in the whole range of the spatial anisotropies. One feature is the nonmonotonic development of the height of the round maximum C_{max} with growing h, which appears in the vicinity of the saturation field. For the model [Eq. (1)], the mean-field theory provides the estimate [27]

$$h_{sat} = 2(1 + R). \tag{2}$$

Another feature is the formation of a second rather sharp peak at the low-temperature side of the aforementioned round maximum which becomes clearly distinguishable at $h = 1.5$ (when considering the density of the h sampling used in the QMC studies) for all anisotropies including $R = 0$ and 1. In the theoretical studies [21,22] of the spin-1/2 HAF chain [i.e., the model given by Eq. (1) for $R = 0$] the sharp maximum was ascribed to the spinon excitations forming particle-hole continua which split in the external magnetic field. At sufficiently strong fields the bandwidths become considerably different, resulting in the two maxima in the specific heat at different temperatures [21]. In the studies of the square lattice in magnetic field, the sharp low-temperature peak has been associated with the binding process of the topological excitations and vortex-antivortex pairs, resulting in the Berezinskii-Kosterlitz-Thouless phase transition [23].

It should be noted that in parallel with the low-temperature specific-heat peak, a sharp anomaly develops also in the

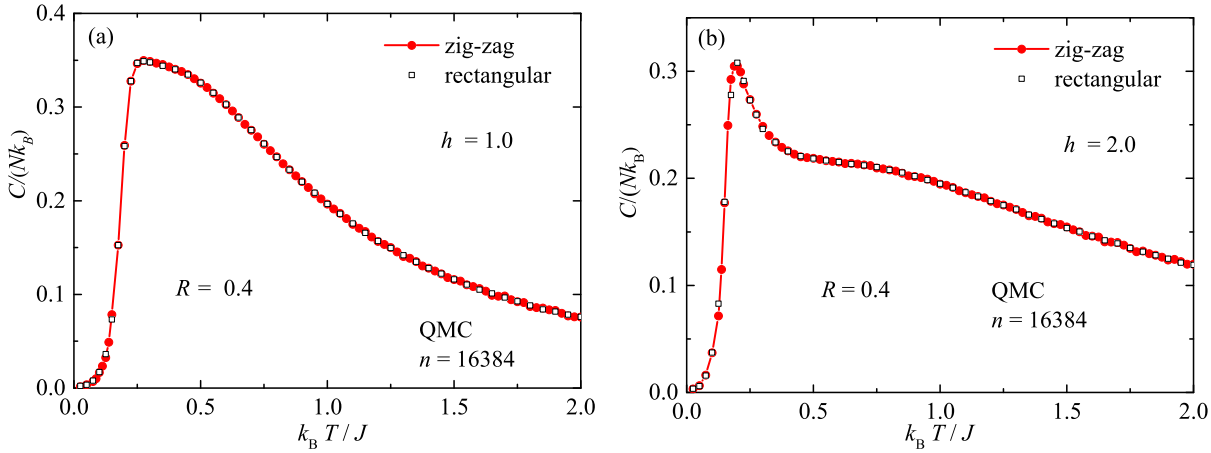

FIG. 5. Temperature dependence of the specific heat of the spin-1/2 HAF on the rectangular and spatially anisotropic zig-zag square lattices with the same number of spins $n = 16384$, calculated for $R = 0.4$ in constant magnetic fields $h = 1.0$ (a) and $h = 2.0$ (b).

susceptibility in the same temperature region for all R values (Figs. 3 and 4). Apparently, some kind of a magnetic-field-induced crossover between 1D and 2D character of excitation spectra may occur, which deserves further studies and is out of the scope of the present paper.

B. Spin-1/2 HAF on the rectangular lattice

Concerning the RL, it has the same coordination number $z = 4$ as the aforementioned ZZL with two pairs of equivalent nearest-neighbor bonds. Both lattices with HAF interactions possess collinear Néel ground states and within the mean-field theory the same saturation fields [1,27]. Therefore, the aim of further numerical studies was to find whether the properties of the two lattices remain equivalent also at finite temperatures and magnetic fields. In the first step, the comparison of available thermodynamic data of RL and ZZL in zero magnetic field was performed and it was found that the temperature dependences of the uniform susceptibilities [3,27] and specific heats [25,27] are the same for both models. In the next step, the thermodynamic quantities of the rectangular lattice with the total number of spins $n = 128 \times 128$ were investigated in magnetic field using the Hamiltonian (1), which can be applied for the rectangular lattice if the first and second summations in Eq. (1) refer to the interaction between nearest neighbors within the same linear chain and the nearest neighbors from different linear chains, respectively.

The comparison of the data for both lattices with the same number of spins suggests that finite-temperature properties remain the same within QMC errors even in the external magnetic field. For illustration, Fig. 5 provides a comparison of RL and ZZL specific heats for $R = 0.4$ in two magnetic fields. Apparent equivalence between both considered models indicates the presence of some sort of hidden symmetry (see the Appendix).

The QMC studies of the temperature dependence of the correlation length ξ in the spin-1/2 HAF on the rectangular lattice revealed growing differences between $\xi^{||}$ (within chains) and $\xi^{\perp}$ (between the chains) for $R \to 0$. Due to large differences ($\xi^{||} > \xi^{\perp}$), the 2D behavior in the RL with small R is observed only at low temperatures and a 2D-1D crossover occurs at higher temperatures [24]. The studies confirmed the reduction of the spin stiffness $\rho_s(R)$ for the increasing spatial anisotropy (i.e., $R \to 0$) and it was found that at intermediate temperatures the QMC data of the correlation length can be described by the relation [31]

$$\xi = A \exp[2\pi \rho_s(R)/k_B T]/\{1 + 0.5 k_B T/[2\pi \rho_s(R)]\}. \quad (3)$$

Besides the spatial anisotropy, the external magnetic field can also reduce the spin stiffness [32,33]. Since a dimensional crossover occurs when the correlation length in one direction becomes of the order of the lattice spacing [24], it can be expected that sufficiently large magnetic field can effectively magnify the spatial anisotropy of the exchange coupling.

Thus, considering the effects of the magnetic field and thermal fluctuations, at least one of the three inequivalent intralayer exchange couplings expected in Cu(en)Cl_2 [Fig. 1 (d)] could be neglected to some extent. Correspondingly, experimental thermodynamic data will be analyzed within the aforementioned models of the spin-1/2 HAF on the rectangular and the zig-zag square lattice which can be treated more or less as effective models due to the reduction of the actual number of the intralayer exchange interactions. Apparently, the analysis cannot discriminate between these models since, as was already demonstrated, both models have the same finite-temperature properties in zero as well as nonzero magnetic field.

IV. RESULTS AND DISCUSSION

A. Specific heat

Temperature dependence of the specific heat of Cu(en)Cl_2 single crystal and polycrystalline Cu(tn)Cl_2 in zero magnetic field is depicted in Fig. 6. The total specific heat of both insulating compounds is composed of the lattice C_{latt} and magnetic C_{mag} contributions. Apparently, the behavior of both contributions is different for each compound. At higher temperatures, where the magnetic contribution is negligible, the larger values of Cu(tn)Cl_2 specific heat indicate that the crystal structure is softer and Debye temperature is lower than in Cu(en)Cl_2. At low temperatures, the magnetic contribution dominates in both compounds, characterized by a round

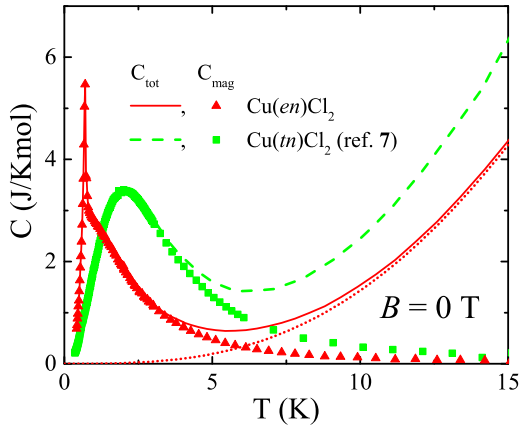

FIG. 6. Temperature dependence of the specific heat of the polycrystalline Cu(*tn*)Cl_2 and single-crystal Cu(*en*)Cl_2 in zero magnetic field. Total and magnetic specific-heat data are represented by lines and symbols, respectively. The dotted line represents the lattice specific heat in Cu(*en*)Cl_2.

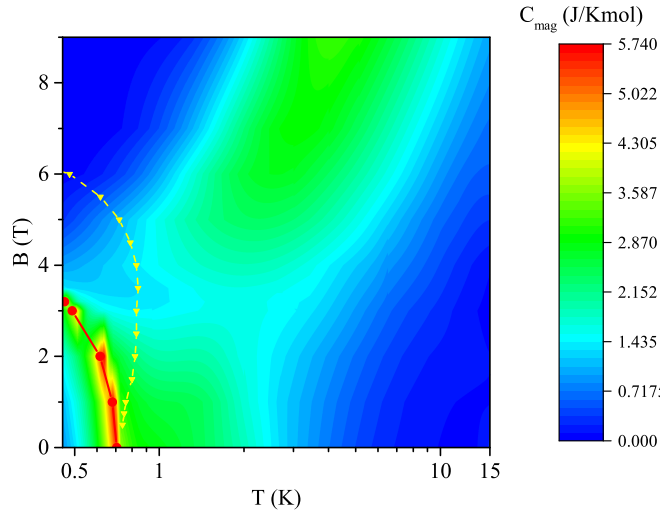

FIG. 7. Temperature dependence of the magnetic specific heat of Cu(*en*)Cl_2 single crystal in magnetic fields applied along the *a* axis. Triangles and circles represent *B*-*T* diagrams of powder Cu(*tn*)Cl_2 [7] and Cu(*en*)Cl_2 in $B|a$, respectively. The lines are guides for the eyes.

maximum, which reflects the presence of short-range magnetic correlations.

In case of Cu(*en*)Cl_2 the shift of the maximum towards lower temperatures suggests significant reduction of the intralayer exchange couplings. What is more, the presence of a sharp λ-like anomaly at $T_N = 0.7$ K clearly marks the onset of the LRO in Cu(*en*)Cl_2.

To analyze the magnetic specific heat of Cu(en)Cl_2 in more detail, the lattice contribution was subtracted using a fitting procedure in the temperature interval from 7 to 15 K. At these temperatures the C_{mag} was approximated by the $1/T^2$ dependence, while a few terms of the low-temperature expansion of C_{latt} within Debye approximation [34] were used. The total specific heat was fitted by the relation $C_{tot}{=}a/T^2 + bT^3 + cT^5 + dT^7$ with $a = 11.47\,\mathrm{J\,K/mol}$, $b = 0.00158\,\mathrm{J/K^4\,mol}$, $c = -1.53 \times 10^{-6}\,\mathrm{J/K^6\,mol}$, and $d = 6.36 \times 10^{-10}\,\mathrm{J/K^8\,mol}$ (Fig. 6). From the parameter *b* the value of Debye temperature was evaluated, $\Theta_D = 109$ K.

After subtracting the lattice contribution, the resulting C_{mag} of Cu(*en*)Cl_2 is depicted in Fig. 6. The total experimental magnetic entropy $S_{tot} = 5.74 \pm 0.05\,\mathrm{J/K\,mol}$ corresponds well to the spin-1/2 system. Despite the strong λ-like anomaly, the compound still preserves two-dimensional character of magnetic correlations as indicated by more than 70% of the magnetic entropy removed above T_N. Such a high ratio is a typical feature of low-dimensional magnets [19].

Depending on the strength of the interlayer coupling, the response of the quasi-low-dimensional magnets on the applied magnetic field can differ. QMC studies of the spin-1/2 HAF on the spatially anisotropic simple cubic lattice in the magnetic field found that for sufficiently weak interlayer coupling the field dependence of the transition temperatures is nonmonotonic [35]. For stronger J', a monotonic decrease of transition temperatures appears characteristic for three-dimensional antiferromagnets [19].

Thus, to obtain more information about the strength of the interlayer coupling in Cu(*en*)Cl_2, the response of the single crystal on the applied magnetic field was investigated.

More specifically, the temperature dependence of the specific heat was measured from 0.4 to 15 K in constant magnetic fields applied parallel to the *a* axis. The data were corrected for the aforementioned lattice contribution (Fig. 7). The mapping of the positions of the λ-like peaks enabled the construction of a magnetic phase diagram. Its similarity with the behavior of the 3D antiferromagnets suggests that in Cu(*en*)Cl_2 the influence of the interlayer coupling is much stronger than in Cu(*tn*)Cl_2. In the latter, the initial shift of a field-induced specific-heat anomaly towards higher temperatures [7] clearly demonstrates a good two-dimensional character of the magnetic lattice (Fig. 7). A simple look at both diagrams suggests a significant reduction of the saturation field in Cu(*en*)Cl_2 resulting from the reduction of 2D magnetic correlations. On the other hand, the extrapolation of the *B*-*T* diagrams towards zero field suggests the existence of the same or very similar ordering temperatures for both compounds. The relation for the transition temperature $T_N = J'(M_{st})^2(\xi/a)^2$ derived for the square lattice [36] (M_{st} and ξ denote the normalized intralayer staggered magnetization and the intralayer correlation length, respectively) suggests that the reduction of 2D correlations indicated in Cu(*en*)Cl_2 requires the enhancement of the interlayer coupling to obtain the same T_N as for Cu(*tn*)Cl_2.

1. Saturation field

QMC calculations of the specific heat presented in Sec. III showed that in the vicinity of the saturation field approached from the low-field side, after initial decrease, the height of a round maximum starts to grow and shift to higher temperatures (Figs. 3 and 4). Such behavior observed in the experimental data (Fig. 7) suggests that B_{sat} can acquire values between 3.5 and 4 T.

Theoretical studies [20] showed that above the saturation field the rise of the aforementioned specific-heat maximum is

governed by the energy gap in the spin excitation spectrum

$$\Delta = g\mu_B(B - B_{\text{sat}}), \tag{4}$$

developing linearly with increasing magnetic field. At temperatures which are sufficiently high for thermal fluctuations to overcome the effects of the interlayer coupling, but small enough with respect to the energy gap ($k_BT < \Delta$), the system approaches with good approximation 2D behavior. Then the magnon spectra acquire 2D character, resulting in the exponential increase of the specific heat [37,38]

$$C_{\text{mag}} \approx \frac{1}{T}\exp(-\Delta/k_BT). \tag{5}$$

Since in the field 4 T the sharp spike in the specific heat vanishes, in the first approximation $B_{\text{sat}} = 4$ T was chosen for a preliminary estimate of the energy gap formed in the highest field 9 T. Using the room-temperature value of the g factor measured along the a axis [15] $g_a = 2.049$, the application of Eq. (4) provided the gap value $\Delta_a/k_B = 6.86$ K. The inspection of the specific heat in 9 T revealed that nonzero contribution of the spin excitations appears above 0.5 K. Using Eq. (5) between 0.5 and 1.8 K yielded the gap value $\Delta_a/k_B = 7.3 \pm 0.1$ K. The corresponding $B_{\text{sat}} = 3.7 \pm 0.1$ T is lower than 4 T but higher than 3.5 T, the field in which the specific heat still shows a significant upturn at lowest temperatures—the sign of the λ-like anomaly occurring outside the experimental temperature window. Thus, a significant reduction of the saturation field compared to Cu(tn)Cl_2 indicates substantial weakening of the intralayer interactions (Fig. 7).

2. *Short-range correlations in B = 0*

Besides rather significant weakening of the intralayer interactions in Cu(en)Cl_2, in zero magnetic field a pronounced λ-like anomaly overlaps the round maximum originating from the short-range order (Fig. 6). QMC simulations of the specific heat of the spin-1/2 HAF on the spatially anisotropic simple cubic lattice [6] showed that the formation of the λ-like anomaly does not lead to the reduction of the 2D round peak. While a weak interlayer coupling has a minimal effect on the round maximum, for the stronger J', the contribution of the interlayer correlations is superimposed on the 2D anomaly.

Considering the aforementioned features, the magnetic specific heat in zero magnetic field was compared with the theoretical predictions for the rectangular lattice with R varying from 0 to 1. The best agreement with the experimental data was found for the models with low R, ranging from 0.1 to 0.4 and $J/k_B = 2.35$ K (Fig. 8). The J parameter corresponds well with the values calculated from Eq. (2). The relation provides for $B_{\text{sat}} = 3.7$ T and $R = 0.1$, 0.2, 0.3, and 0.4 the intrachain coupling $J/k_B = 2.31$, 2.12, 1.95, and 1.81 K, respectively. The deviations of the experimental data from the aforementioned theoretical 2D anomalies below $k_BT/J < 0.75$ could be ascribed to the effect of the third interaction, which was omitted in the analysis.

As was shown in Ref. [39], the presence of the additional NNN interaction in the spin-1/2 HAF square lattice significantly changes finite-temperature properties. When the NNN coupling becomes larger, the corresponding round specific-heat anomaly decreases and shifts towards lower temperatures

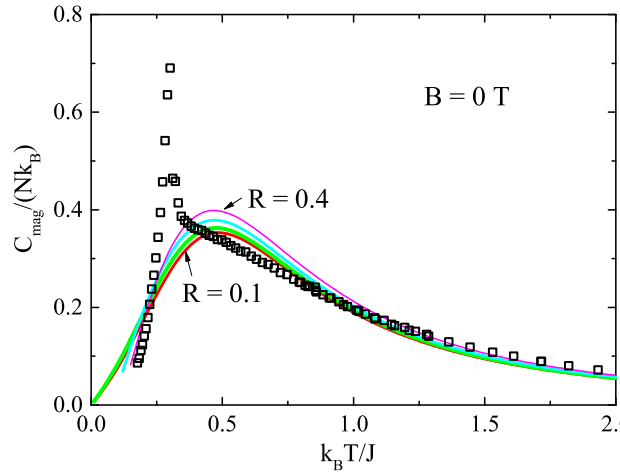

FIG. 8. Temperature dependence of the magnetic specific heat of Cu(en)Cl_2 in zero magnetic field (squares) compared with the QMC calculations [25] of the specific heat of the spin-1/2 HAF on the rectangular lattice with $R = 0.1$, 0.2, 0.3, and 0.4 and $J/k_B = 2.35$ K.

[39]. Thus, a similar effect can be expected also in the rectangular lattice with the NNN coupling as expected in Cu(en)Cl_2 [Fig. 1(d)].

3. *Magnetic entropy and short-range correlations in B > 0*

Concerning the effect of long-range correlations, the magnetic entropy removed below the phase transition, S_c^{3D}, rapidly decreases with growing magnetic field. In the reduced coordinates the curves C/C_{max}^{3D} vs T/T_c (C_{max}^{3D} represents the height of the λ-like anomaly at the transition temperature T_c for a given magnetic field) fall on one universal curve below the phase transition (Fig. 9). On the other hand, in the paramagnetic phase, the interplay of short-range correlations and magnetic field is apparent up to about 2–3T/T_c. At higher temperatures, the effect of magnetic field dominates, reflected by rising specific-heat values in higher magnetic fields.

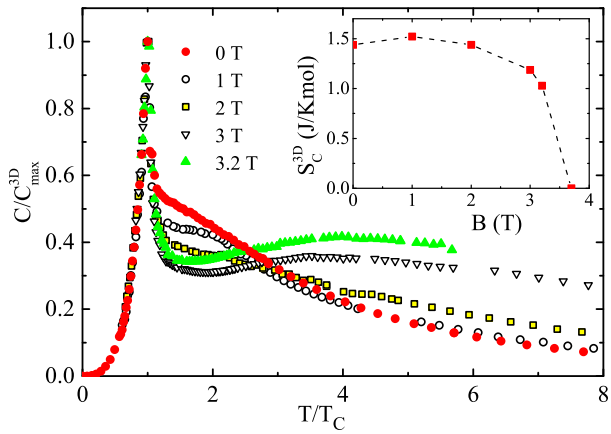

FIG. 9. Temperature dependence of the magnetic specific heat of Cu(en)Cl_2 in reduced coordinates. Inset: Magnetic field dependence of the magnetic entropy removed below the phase transition.

The specific heat in zero magnetic field can be well extrapolated down to zero temperature with the T^3 dependence which enabled corresponding extrapolation of the universal curve down to $T/T_c = 0$ (Fig. 9). Thus, despite the limited experimental temperature window, the universal specific-heat behavior below the phase transition enabled us to evaluate the magnetic entropy S_c^{3D} in all magnetic fields where the λ-like anomaly is observable. The evaluation of the magnetic entropy from the universal curve

$$S_c^{3DRed} = \int_0^1 \frac{\left(C/C_{max}^{3D}\right)}{(T/T_c)} d(T/T_c) \tag{6}$$

yielded dimensionless $S_c^{3DRed} = 0.26 \pm 0.01$ which enabled us to calculate the real magnetic entropy S_c^{3D} in the given field

$$S_c^{3D}(B) = S_c^{3DRed} C_{max}^{3D}(B). \tag{7}$$

Apparently, the relative change of the magnetic entropy correlates with the relative change of the specific-heat maxima at the transition temperatures (Fig. 9, inset). Within the experimental inaccuracy (about 5% at T_c), the $S_c^{3D}(B)$ vs B dependence scales with the T_c vs B magnetic phase diagram in Fig. 7.

Above the saturation field the ground state consists of all spins up, which corresponds to a ferromagnet in the magnetic field [40]. In this field region, the specific heat is not distorted by the λ-like anomaly and the analysis within the effective 2D model [Eq. (1)] can be performed. Concerning the specific heat in the field 4 T, the estimation of the magnetic entropy in the whole temperature range provided $S_{mag} = 5.7 \pm 0.1$ J/K mol, which is close to the Rln2 value for the spin 1/2. Considering the values of the intrachain exchange couplings derived from the saturation field [Eq. (2)] in Sec. IV A 2, the field 4 T corresponds to $h = 2.38, 2.58$, and 3.00 for $R = 0.1, 0.2$, and 0.4, respectively. The first two values are close to the value 2.5, for which QMC specific-heat data (Sec. III) are available. The comparison of the corresponding QMC simulations and the experimental data in the field 4 T is depicted in Fig. 10. Apparently, the best agreement can be found for $R \approx 0.2$ after rescaling J/k_B to 2.35 K to fit the position of the maximum.

To verify the credibility of the B_{sat} estimated from the low-temperature specific-heat data in 9 T using Eq. (5), the experimental as well as the QMC specific-heat data for $R = 0.2$ were drawn in the reduced coordinates C^h/C_{max}^h vs T^h/T_{max}^h (C_{max}^h and T_{max}^h represent the height and the position of the round maximum in the field h, respectively). Naturally, the experimental and theoretical plots were constructed only for the fields in which the round maximum appears. For completeness, the specific heat of the spin-1/2 paramagnet in the magnetic field (i.e., two-level system) as a limiting case $h \to \infty$ has been also added (Fig. 11). The inspection of the theoretical plots in Fig. 11(a) revealed largest deviations from the paramagnet curve for $h = 2.0$ and 2.5. For increasing fields above $h_{sat} = 2.4$, a gradual shrinking of the curves towards the paramagnet curve is observed. The same behavior was observed for other R values and a similar tendency can also be seen in the plot of the experimental data, where the largest deviations from the paramagnet curve occur for the fields 3.5 and 4 T [Fig. 11(b)].

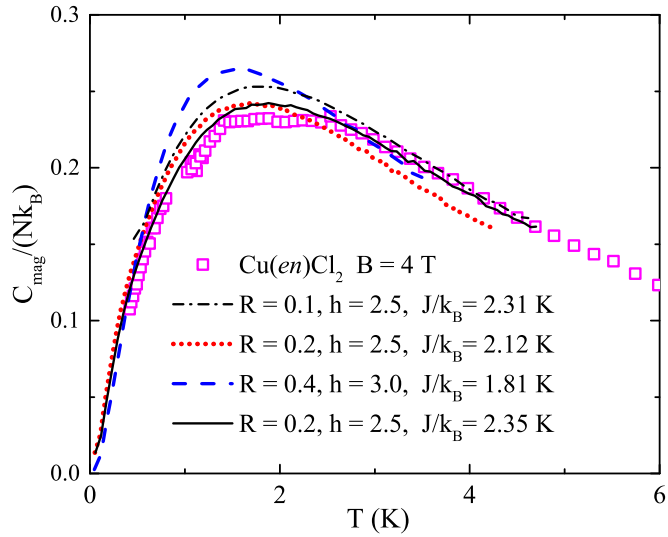

FIG. 10. Temperature dependence of the magnetic specific heat of Cu(*en*)Cl_2 in the field 4 T applied along the a axis (symbols). The lines represent QMC data for the spin-1/2 HAF on the rectangular lattice with the linear size $L = 128$ for various R.

Apparently, the plot of the experimental data in the reduced coordinates offers the alternative method for the estimation of the saturation field even at moderate temperatures. Besides the disappearance of the low-temperature (LRO or 2D in nature) spike, the closeness of the saturation field is manifested by the maximum deviations from the paramagnet curve.

In addition, the inspection of the C^h/C_{max}^h vs T^h/T_{max}^h plots for all R values revealed that in the growing magnetic field, after initial decrease and flattening, the formation of a separate round maximum begins in the fields above $\approx 0.75 h_{sat}$. This feature could be associated with the onset of a strong-field region theoretically predicted for the spin-1/2 HAF on the square lattice in the fields ranging between $h^* \approx 0.75\, h_{sat}$ and h_{sat} [33,41]. In these fields, the instability of antiferromagnetic magnons occurs, which spreads gradually through enlarging portions of the Brillouin zone when h approaches h_{sat}. The threshold field h^* occurs in all antiferromagnets with the ordered ground state irrespective of their dimensionality, spin value, or the type of the order [41,42].

As a finite-temperature indicator of the strong-field region, the reduced entropy of the 2D system described by Eq. (1) was chosen:

$$S^{2DRed}(h) = \int_0^\infty \frac{\left(C^h/C_{max}^h\right)}{\left(T^h/T_{max}^h\right)} d\left(T^h/T_{max}^h\right). \tag{8}$$

Applying the relation analogic to Eq. (7),

$$S^{2D}(h) = S^{2DRed}(h) C_{max}^h, \tag{9}$$

the real magnetic entropy $S^{2D}(h)$ in the whole temperature range is always equal to ln(2) for the spin 1/2. For $R = 0.2$, $S^{2DRed}(h) = 1.915, 1.925, 2.016, 2.358, 3.357$, and 2.860 for $h = 0, 0.2, 0.5, 1, 2$, and 2.5, respectively. The parameter $S^{2DRed}(h)$ does not achieve maximal value at $h = h_{sat}$, as one would intuitively expect. Instead, within the h sampling, the maximal value is achieved for $h = 2$, which is about 0.83 h_{sat}. A similar conclusion is valid for all other R values.

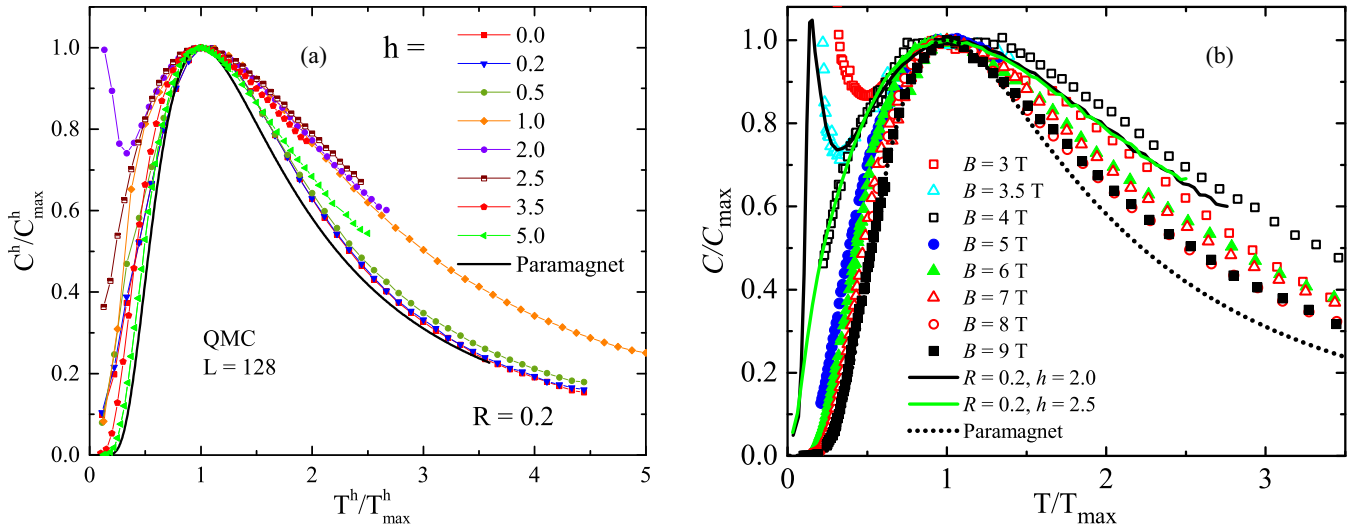

FIG. 11. (a) Temperature dependence of the specific heat of the spin-1/2 HAF on the rectangular lattice ($R = 0.2$) in various fields. (b) Temperature dependence of the magnetic specific heat of Cu(*en*)Cl_2 in various fields applied along the *a* axis (symbols). The solid lines represent QMC data for the spin-1/2 HAF on the rectangular lattice ($R = 0.2$) in the magnetic fields $h = 2$ and 2.5. The dotted line corresponds to the spin-1/2 paramagnet in the magnetic field.

For completeness, the $S = 1/2$ paramagnet in field is also enclosed, with $S^{2DRed} = 1.578$. The aforementioned behavior of the specific heat and the reduced entropy suggests that these finite-temperature properties seem to be sensitive to the onset of the high-field regime. Further QMC calculations would be useful to investigate the finite-temperature properties in the strong-field region in detail.

Concerning Cu(*en*)Cl_2, the appearance of a separate round maximum in the specific heat at 3 T $\approx 0.8\,B_{sat}$ suggests the onset of the high-field regime. The gradual prevailing effect of the magnetic field over the interlayer correlations can be seen in the development of the specific heat. The comparison of the experimental data with the 2D model of the spin-1/2 HAF on the rectangular lattice with $R = 0.2$ reflects this tendency (Fig. 12). While in the fields below 3 T the discrepancies between the data and the theory are large, in higher fields, the agreement improves. The values of normalized fields h_0 for the individual sets of experimental data were calculated for a given magnetic field B and $J/k_B = 2.35$ K and are depicted in Fig. 12 in the frame. Subsequently, the QMC data for $R = 0.2$ and h values close to h_0 were chosen for the comparison with the experimental data.

B. Magnetization

1. *Magnetic field dependence of magnetization*

Isothermal magnetization curves were investigated at 0.45 K and magnetic fields up to 5 T applied along the *a*, *b*, and c^* axes [Fig. 13(a)]. In the highest fields the magnetization achieves nearly saturated values, which were used for a lower estimate of *g*-factor values in all three directions. The prescription for the saturation value $M_{sat} = Ng\mu_B S^z$ for the spin 1/2 provides $g_a = 2.09 \pm 0.01$, $g_{c^*} = 2.08 \pm 0.01$, and $g_b = 2.21 \pm 0.01$. The estimates correspond to the room-temperature values $g_a = g_{c^*} = 2.049 \pm 0.010$ and $g_b = 2.239 \pm 0.010$ obtained within the electron paramagnetic resonance experiment [15]. Using the low-temperature *g* factors, the rescaling of the magnetization data provided a universal curve $M/Ng\mu_B$ vs $g\mu_B B/J$. The best agreement with the theoretical prediction for the spin-1/2 HAF on the rectangular lattice was achieved for $R = 0.2$ and $J/k_B = 2.20$ K [Fig. 13(a)]. A slightly different J value obtained from the analysis of the magnetization can be ascribed to the combined effect of the interlayer correlations dominating at low fields and the neglecting of the weakest third exchange coupling. The discrepancy between the theory and the data in the vicinity of the saturation field can be ascribed to the effect of a finite temperature; the QMC data were calculated at $k_B T/J = 0.1$, while the experimental data were measured at $k_B T/J \approx 0.2$.

Considering $h_{sat} = 2.4$ for the spin-1/2 HAF on the rectangular lattice with $R = 0.2$ and using $J/k_B = 2.20$ K and the *g* factors estimated from the magnetization, the saturation fields were evaluated for the individual field orientations, $B^a_{sat} \approx B^{c^*}_{sat} = 3.77 \pm 0.05$ T and $B^b_{sat} = 3.57 \pm 0.05$ T.

Concerning the strong-field region, the exact diagonalization studies of the spin-1/2 HAF on the square lattice [33] at zero temperature revealed that high-energy magnons in the vicinity of the (π, π) point in the Brillouin zone become unstable when the uniform magnetization achieves the value $m_c \approx 0.3$ which corresponds to the aforementioned h^*. The inspection of the experimental data in [Fig. 13(a)] revealed that the reduced magnetization achieves the value $m \approx 0.3$ at $h \approx 1.9$. For the rectangular lattice with $R = 0.2$ the value corresponds to 0.79 h_{sat}, which is rather close to h^*. Thus, considering easy access to the strong-field region, Cu(*en*)Cl_2 can potentially serve as a good candidate for the investigation of the instabilities of the one-magnon spectra.

Besides the strong-field region, a closer look at the magnetization data revealed anomalous behavior in low fields $h < 0.2$ manifested by slight deviations from the initial linear dependence [Fig. 13(b)]. The deviations occur at about 100–150 mT in the field oriented along the *a* axis, while some indications appear also along the c^* direction in the

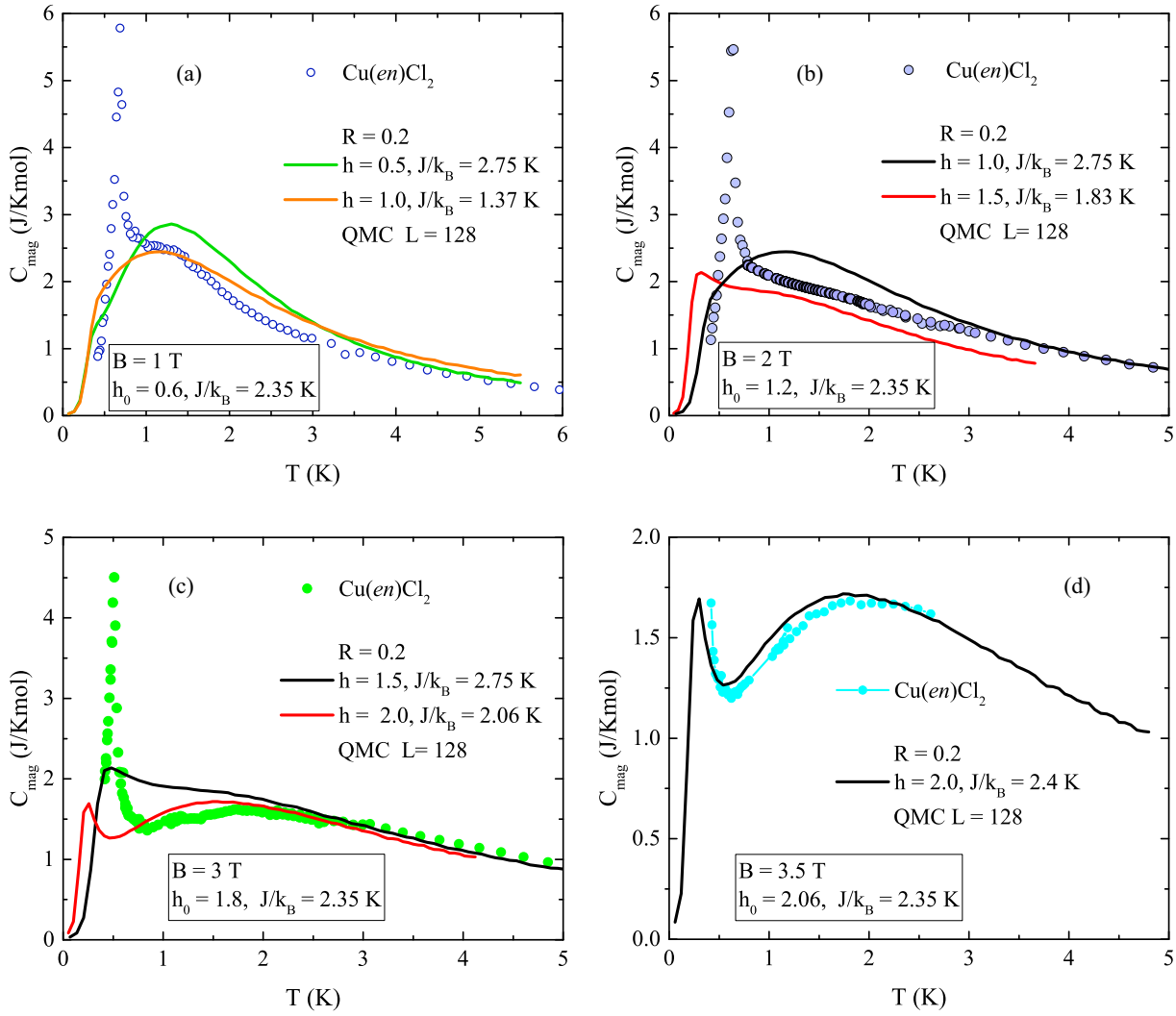

FIG. 12. Temperature dependence of the magnetic specific heat of Cu(*en*)Cl_2 in the magnetic field 1 T (a) 2 T (b) 3 T (c) and 3.5 T (d) applied along the *a* axis (symbols). Solid lines represent QMC data ($L = 128$) for the spin-1/2 HAF on the rectangular lattice with $R = 0.2$ in various fields. The values of the normalized fields $h_0 = g\mu_B B/J$ calculated for a given field B and $J/k_B = 2.35$ K are shown in the frame.

same field region exhibiting some features characteristic for the spin-flop transition. The low-field anomalies are not so noticeable as those associated with the spin-flop transitions observed in other low-dimensional Cu(II)-based quantum magnets [2,27,43]. Similar features characteristic of the spin-flop transition, i.e., the observation of the anomalous magnetization behavior in two directions, were ascribed to the misalignment between the magnetic field and the easy axis [44]. The investigation of the angular dependence of the spin-flop transition in 2D and 3D antiferromagnets revealed that the spin-flop transition extends for large angles between the field and the easy axis [43,45]. The room-temperature electron paramagnetic resonance and polarized electronic spectra suggest that in Cu(*en*)Cl_2 the local anisotropy axes *x, y,* and *z* coincide with the symmetry of the CuN_2Cl_4 chromophore [16]. While the *z* axis coincides with the crystallographic *b* axis, *x* and *y* axes lie close to the bond directions of the chromophore. In this respect, the crystallographic *a* and *c* axes are tilted from the *x* and *y* axes by the angle $\approx 30°$, respectively [16]. Considering these facts, the slightly stronger anomaly along the *a* axis suggests that the *x* axis should be the easy axis, while the *y* axis and *z* axis stand for the middle and hard axis, respectively.

To verify this conjecture, the magnetization was carefully investigated in very low magnetic fields ranging from −20 to 20 mT to exclude any effect of the spin-flop transition. The "hysteresis loops" in all three directions (i.e., the sequence $0 \rightarrow 20 \rightarrow -20 \rightarrow 20$ mT) lack any hysteresis and are strictly linear, indicating the absence of any weak ferromagnetism (Fig. 14, inset). Within the mean-field theory, it was shown that at zero temperature and magnetic fields below the spin-flop transition the normalized magnetization along the hard axis grows faster than that along the middle axis, while the magnetization along the easy axis remains zero [27]. Thus, considering finite-temperature effects and the expected tilting, the normalized experimental magnetization data in the mT region support the aforementioned conjecture that the *b* axis corresponds to the hard axis *z,* while the *a* and *c** directions lie closer to the easy *x* axis and middle *y* axis, respectively.

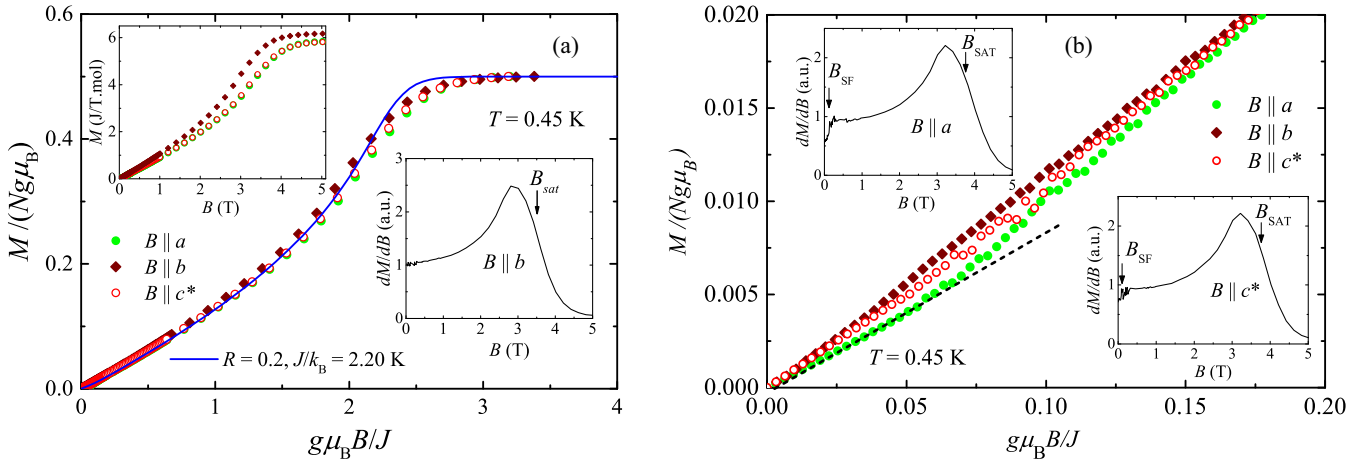

FIG. 13. (a) Magnetic field dependence of the isothermal magnetization of Cu(*en*)Cl_2 in the field applied along the *a*, *b*, and c^* axes at 0.45 K depicted in the reduced coordinates (symbols). The solid line represents QMC data ($L = 128$) for the spin-1/2 HAF on the rectangular lattice with $R = 0.2$ and $J/k_B = 2.20$ K at the constant temperature $k_BT/J = 0.1$. Upper inset: Magnetic field dependence of the isothermal magnetization of Cu(*en*)Cl_2 in the field applied along the *a*, *b*, and c^* axes at the constant temperature 0.45 K. Lower inset: Derivative of the isothermal magnetization at 0.45 K in the field $B||b$. (b) The same data as in the main figure (a) shown in the low-field region (symbols). The dashed line demonstrates the deviation of the magnetization data from the linear behavior, measured in $B||a$. Upper and lower inset: Derivative of the isothermal magnetization at 0.45 K in the field $B||a$ and $B||c^*$, respectively. The arrows denote the saturation and spin-flop fields (see text).

2. *Temperature dependence of magnetization*

Temperature dependence of magnetization was investigated at temperatures from 0.45 to 1.8 K in magnetic fields applied along the *a*, *b,* and c^* direction, ranging from 5 to 40 mT. The measurements were performed in both ZFC and FC regimes. The coincidence of the FC and ZFC data even below the phase transition to the long-range magnetic order and the aforementioned shape of the "hysteresis loops" [Fig. 14(a)] indicate the absence of weak ferromagnetism in Cu(*en*)Cl_2, which could be related with the Dzialoshinkii-Moriya interaction or some other sources. For a given orientation of the magnetic field the normalization *M(T)/B* provides the same curve for all aforementioned magnetic fields. Therefore, in further analysis the *M(T)/B* data were treated as the initial magnetic susceptibility χ.

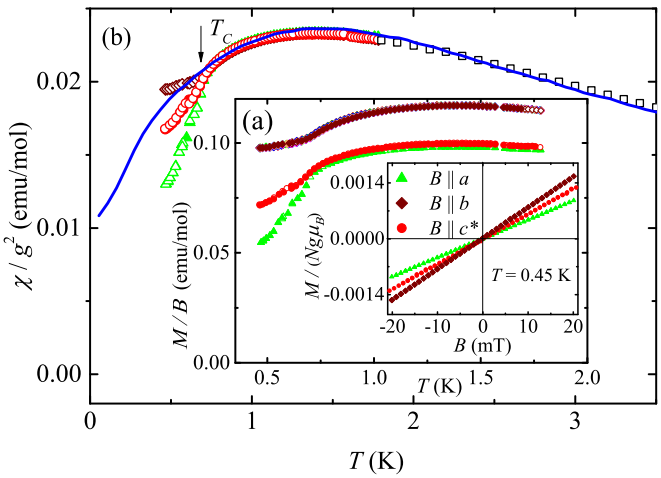

FIG. 14. (a) Temperature dependence of the normalized magnetization *M/B* of Cu(*en*)Cl_2 in constant fields applied along the *a*, *b*, and c^* axes. FC (ZFC) data are represented by full (open) symbols. For illustration, in $B|b$, the data in all fields (5, 10, 15, 20, 30, and 40 mT) are included, while in $B|a, c^*$ for clarity only the data in $B = 40$ mT are depicted. Inset: "Hysteresis loops" of normalized magnetization $M/(Ng\mu_B)$ vs *B* at the constant temperature $T = 0.45$ K. (b) The same data as in the main figure (a) divided by $g^2(M/(Bg^2) \equiv \chi(T)/g^2)$ with $g_a = 2.12$, $g_{c^*} = 2.11$, $g_b = 2.24$. For clarity, only ZFC and FC data at 40 mT are selected for each orientation. The high-temperature data above 1.8 K (open squares) are powder data taken from Ref. [17] and divided by the reported $g = 2.01$. The solid line represents the QMC data ($L = 128$) for the spin-1/2 HAF on the rectangular lattice in zero magnetic field with $R = 0.2$ and $J/k_B = 2.18$ K.

To exclude the effect of the *g*-factor anisotropy, the experimental susceptibility data in each orientation were divided by the square of the corresponding *g* factor. The values $g_a = 2.12$, $g_{c^*} = 2.11$, and $g_b = 2.24$ were chosen to obtain a universal normalized curve above the phase transition, where the spin isotropic 2D behavior can be expected [46]. For temperatures above 1.8 K, the powder susceptibility data taken from Ref. [17] with the reported $g = 2.01$ were used [Fig. 14(b)]. It can be seen that such normalization provides a universal curve above the phase transition, while below $T_N = 0.7$ K the curve splits into three lines with the behavior typical for the magnet with the orthorhombic spin anisotropy. Applying the theoretical results for the susceptibility of the spin-1/2 easy-axis XXZ model on the square lattice below the phase transition [46], in the case of Cu(*en*)Cl_2, χ_a below T_N corresponds to the susceptibility along the easy axis, while χ_b behaves as the susceptibility along the hard axis, in coincidence with the isothermal magnetization curves [Fig. 14(a), inset]. The experimental data above the phase transition were compared with the QMC data ($L = 128$) for the spin-1/2 HAF on the rectangular lattice with $R = 0.2$ in zero magnetic field and the best agreement was found for $J/k_B = 2.18 \pm 0.05$ K.

V. CONCLUSIONS

The interplay of the magnetic field and interlayer correlations was experimentally investigated in a quasi-two-dimensional quantum magnet Cu(*en*)Cl_2. The analysis of the crystal structure suggests the presence of three different intralayer exchange interactions forming a rectangular lattice with a coupling along one of the diagonals within the rectangular plaquettes. When any of the three interactions is neglected, the lattice transforms into the rectangular or the spatially anisotropic zig-zag square lattice, both with nearest-neighbor interactions.

These two models served as the effective models for the analysis of the experimental specific heat and magnetization. For that purpose, QMC calculations of the thermodynamic quantities were performed for the spin-1/2 HAF on the rectangular and the spatially anisotropic zig-zag square lattice in the wide range of parameters enabling detailed mapping of finite-temperature properties of both models. The calculations showed that within QMC errors the finite-temperature properties of both models are identical for the same parameters. Subsequent analysis of the vertex symmetry confirmed the equivalency of both lattices. In addition, the equivalency with other 2D lattices with four nearest neighbors was revealed.

The comparison of the Cu(*tn*)Cl_2 and Cu(*en*)Cl_2 specific heats in zero magnetic field as well as corresponding magnetic phase diagrams revealed that the $tn \rightarrow en$ substitution significantly reduced the strength of the intralayer interactions in Cu(*en*)Cl_2 and enhanced the influence of the interlayer correlations. This significant change was manifested by the clear observation of a phase transition to the long-range order at 0.7 K in zero magnetic field and a significant reduction of the saturation field compared to its *tn* counterpart.

To exclude the effect of the long-range correlations, which strongly screen the manifestation of the 2D SRO in zero magnetic field, the specific heat in the magnetic field of 9 T was analyzed to provide the estimate $B_{\mathrm{sat}} \approx 3.7\,\mathrm{T}$. The saturation field value combined with the general theoretical conclusions about the specific-heat behavior affected by the interlayer coupling and the next-nearest-neighbor interactions in the spin-1/2 HAF on the square lattice served as important constraints for the selection of a proper magnetic model for Cu(*en*)Cl_2. Then using the wide set of the QMC specific-heat data for various strengths of the spatial anisotropy, magnetic fields, and temperatures, these constraints enabled us to narrow the selection to the model of the rectangular and zig-zag square lattice with $R \approx 0.2$ and the intralayer coupling $J/k_{\mathrm{B}} \approx 2.3\,\mathrm{K}$. These parameters were further successfully used for the description of the isothermal magnetization at 0.45 K and the initial magnetic susceptibility both measured in three field orientations.

The inspection of the isothermal magnetization data at 0.45 K in the low-field region revealed the characteristics recalling the spin-flop transition in the field about 100 mT. The observation of the anomalous behavior in two orientations was ascribed to the deviation of the crystallographic axes from the local anisotropy axes. The character of the "hysteresis loops" investigated in the mT region at 0.45 K as well as the magnetic susceptibility studied in the magnetic fields far below the spin-flop transition exclude the presence of a weak ferromagnetism originating from the Dzialoshinskii-Moriya interaction or other sources. On the other hand, both sets of the experimental data point tp the presence of the symmetric spin anisotropy of the rhombic symmetry.

Despite the large influence of the interlayer coupling and rather complicated distribution of intralayer exchange pathways, considering the constraints as the saturation field, the effect of the interlayer and intralayer interactions, and the availability of a sufficient number of various theoretical predictions, the analysis showed the possibility to extract the main features of the low-dimensional magnetic subsystem in Cu(*en*)Cl_2 from rather simple and easy-accessible measurements as the specific heat and magnetization.

Besides the aforementioned rather successful identification of the 2D quantum magnet, some other issues should be addressed in future. The behavior of the low-temperature properties of the models in magnetic field suggests some kind of crossover in the character of the excitation spectra when the spatial anisotropy varied from $R = 0$ to 1. Last but not least, the behavior of a reduced entropy, the special parameter depending on the given 2D model characterized by R and the reduced magnetic field h, suggests that the reduced entropy achieves maximum values for the fields close to the threshold field h^*, at least within the h sampling used in the QMC calculations. In this respect, Cu(*en*)Cl_2 with its low saturation field represents a 2D system in which the strong-field regime is easily accessible and together with the availability of quality single crystals it can be a useful candidate for the experimental investigation of the magnon instabilities as predicted theoretically for the spin-1/2 HAF on the square lattice in the magnetic fields above h^*.

ACKNOWLEDGMENTS

The work has been supported by VEGA Grant No. 1/0269/17 of the Scientific Grant Agency of the Ministry of Education, Science, Research and Sport of the Slovak Republic and the Slovak Academy of Sciences and the Slovak Research and Development Agency Projects No. APVV-18-0197, No. APVV-14-0078, No. APVV-16-0186 and No. APVV-14-0073.

APPENDIX: EQUIVALENCE OF THE RECTANGULAR AND THE SPATIALLY ANISOTROPIC ZIG-ZAG SQUARE LATTICE

The main idea of the equivalence between the anisotropic zig-zag lattice and the rectangular lattice shown in Fig. 15 is discussed for the spin-1/2 HAF model. On both lattices, the model can be exactly decomposed into identical smaller blocks, so-called local Hamiltonians, which are described by three nearest-lying spin sites (i.e., three spins forming the right angle). The examples of the three-spin local Hamiltonians $H^A_{i,j}$ and $H^B_{i+1,j}$ are depicted in Fig. 16.

In this manner, the two local Hamiltonians can build up the entire lattices, as schematically shown in Fig. 17 for both of the lattice types. Evidently, the zig-zag lattice requires mapping of the two local Hamiltonians $H^A_{i,j}$ and $H^B_{i+1,j}$ in the alternating (chessboard) pattern, whereas the rectangular lattice needs only one type of the local Hamiltonian, say $H^A_{i,j}$, in this particular case. Notice that the middle spin of the local

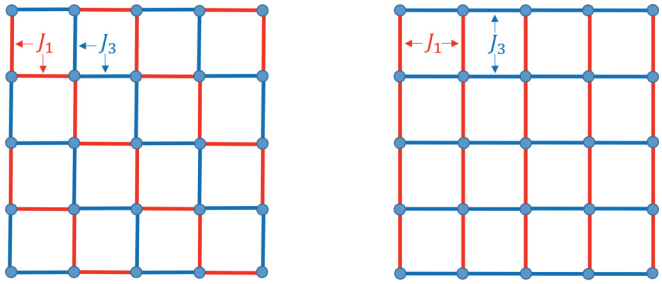

FIG. 15. (a) The zig-zag lattice is characteristic for the alternating interactions J_1 (red) and J_3 (blue) along the vertical and horizontal directions. (b) The rectangular lattice exhibits the vertical $J_1 = J$ (red) and the horizontal $J_3 = RJ$ (blue) interactions being fixed for the entire lattice.

Hamiltonians $H^A_{i,j}$ and $H^B_{i+1,j}$ specifies the lattice positions i and j (Fig. 17).

First, let us consider a uniform decomposition of the rectangular lattice, as in Fig. 17(b), into the identical local Hamiltonians $H^A_{i,j}$. It means that the total Hamiltonian $H_{\rm tot}$ of the HAF model, being fully specified by Eq. (1), can be decomposed in this way:

$$H_{\rm tot} = \sum_{i=1}^{N}\sum_{j=1}^{M} H^A_{i,j} = \sum_{i=1}^{N}\sum_{j=1}^{M}\big[J_1\,\vec{\mathbf{S}}_{i,j+1}\cdot\vec{\mathbf{S}}_{i,j} + J_3\,\vec{\mathbf{S}}_{i,j}\cdot\vec{\mathbf{S}}_{i+1,j} - h\big(S^z_{i,j+1} + S^z_{i,j} + S^z_{i+1,j}\big)\big]. \tag{A1}$$

Clearly, $H^A_{i,j}$ coincides with the scheme depicted in Fig. 16(a). Since each of the three spins in $H^A_{i,j}$ is equally shared with the spin in the surrounding local Hamiltonians, we have to rescale the constant magnetic field by the factor of 1/3. Then, the magnetic field $h = g\mu_B B/3$ can completely reproduce the original $H_{\rm tot}$.

In general, the HAF model can be defined on a rectangular lattice system of size $N \times M$ (where N and M are assumed to be even numbers). We imposed the periodic boundary conditions on both lattice types in order to unify the boundary spins, which have to satisfy the cyclic condition $\vec{\mathbf{S}}_{N+1,j} = \vec{\mathbf{S}}_{1,j}$ and $\vec{\mathbf{S}}_{i,M+1} = \vec{\mathbf{S}}_{i,1}$.

We can analogously decompose the total Hamiltonian of the zig-zag lattice [see Fig. 17(a)] into the sum of the two

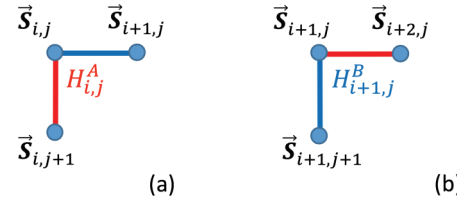

FIG. 16. The two neighboring three-spin blocks described by the local Hamiltonians: (a) $H^A_{i,j}$ and (b) $H^B_{i+1,j}$.

alternating local Hamiltonians $H^A_{i,j}$ and $H^B_{i,j}$:

$$H_{\rm tot} = \sum(H^A + H^B) = \sum_{\alpha=1}^{2}\sum_{i=0}^{N/2}\sum_{j=0}^{M/2}\big(H^A_{2i+\alpha,2j+\alpha} + H^B_{2i+\alpha,2j+\alpha+1}\big). \tag{A2}$$

We can express the Hamiltonian (A2) in a simpler form, in which the four neighboring local Hamiltonians are grouped into a 3×3 square-lattice block of spins:

$$H_{\rm tot} = \sum_{i,j=0}^{N/2,\,M/2}\big(H^A_{2i,2j} + H^B_{2i+1,2j} + H^A_{2i+1,2j+1} + H^B_{2i,2j+1}\big), \tag{A3}$$

where, after renaming $2i \to i$ and $2j \to j$, in accord with Fig. 16(a), we get

$$H^A_{i,j} = J_1\,\vec{\mathbf{S}}_{i,j+1}\cdot\vec{\mathbf{S}}_{i,j} + J_3\,\vec{\mathbf{S}}_{i,j}\cdot\vec{\mathbf{S}}_{i+1,j} - h\big(S^z_{i,j+1} + S^z_{i,j} + S^z_{i+1,j}\big) \tag{A4}$$

and [compare with Fig. 16(b)]

$$H^B_{i+1,j} = J_3\vec{\mathbf{S}}_{i+1,j+1}\cdot\vec{\mathbf{S}}_{i+1,j} + J_1\vec{\mathbf{S}}_{i+1,j}\cdot\vec{\mathbf{S}}_{i+2,j} - h\big(S^z_{i+1,j+1} + S^z_{i+1,j} + S^z_{i+2,j}\big). \tag{A5}$$

If replacing all the local terms H^B with H^A in Eq. (A3), we recover the original rectangular lattice [Eq. (A1)]. This replacement is equivalent to exchanging the interactions J_1 and J_3. In other words, we intend to analyze the exchange of J_1 and J_3 in order to specify the conditions under which the two local Hamiltonians (A4) and (A5) shown in Figs. 16(a) and 16(b) are exchangeable. Then, we only need to compare

$$H^A_{i,j} = J_1(\vec{\mathbf{S}}_{i,j+1}\cdot\vec{\mathbf{S}}_{i,j}) + J_3(\vec{\mathbf{S}}_{i,j}\cdot\vec{\mathbf{S}}_{i+1,j}) - h\big(S^z_{i,j+1} + S^z_{i,j} + S^z_{i+1,j}\big),$$
$$H^B_{i,j} = J_3(\vec{\mathbf{S}}_{i,j+1}\cdot\vec{\mathbf{S}}_{i,j}) + J_1(\vec{\mathbf{S}}_{i,j}\cdot\vec{\mathbf{S}}_{i+1,j}) - h\big(S^z_{i,j+1} + S^z_{i,j} + S^z_{i+1,j}\big). \tag{A6}$$

Having expressed $H^A_{i,j}$ in the matrix formalism, we obtain

$$H^A_{i,j} = \begin{pmatrix}
J_1+J_3-3h & 0 & 0 & 0 & 0 & 0 & 0 & 0\\
0 & J_3-J_1-h & 2J_1 & 0 & 0 & 0 & 0 & 0\\
0 & 2J_1 & -J_1-J_3-h & 0 & 2J_3 & 0 & 0 & 0\\
0 & 0 & 0 & J_1-J_3+h & 0 & 2J_3 & 0 & 0\\
0 & 0 & 2J_3 & 0 & J_1-J_3-h & 0 & 0 & 0\\
0 & 0 & 0 & 2J_3 & 0 & -J_1-J_3+h & 2J_1 & 0\\
0 & 0 & 0 & 0 & 0 & 2J_1 & J_3-J_1+h & 0\\
0 & 0 & 0 & 0 & 0 & 0 & 0 & J_1+J_3+3h
\end{pmatrix}$$

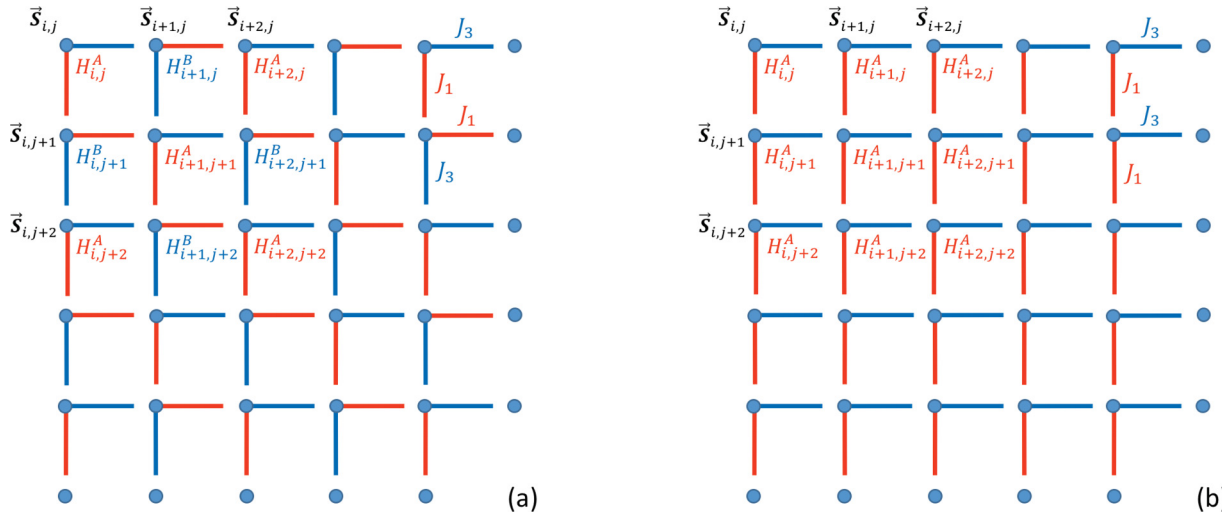

FIG. 17. (a) The anisotropic zig-zag lattice and (b) the topologically equivalent rectangular lattice (see Fig. 15).

and for $H^B_{i,j}$ we get

$$H^B_{i,j} = \begin{pmatrix} J_1+J_3-3h & 0 & 0 & 0 & 0 & 0 & 0 & 0 \\ 0 & J_1-J_3-h & 2J_3 & 0 & 0 & 0 & 0 & 0 \\ 0 & 2J_3 & -J_1-J_3-h & 0 & 2J_1 & 0 & 0 & 0 \\ 0 & 0 & 0 & J_3-J_1+h & 0 & 2J_1 & 0 & 0 \\ 0 & 0 & 2J_1 & 0 & J_3-J_1-h & 0 & 0 & 0 \\ 0 & 0 & 0 & 2J_1 & 0 & -J_1-J_3+h & 2J_3 & 0 \\ 0 & 0 & 0 & 0 & 0 & 2J_3 & J_1-J_3+h & 0 \\ 0 & 0 & 0 & 0 & 0 & 0 & 0 & J_1+J_3+3h \end{pmatrix}$$

After rewriting these two matrices into the block-diagonal form with respect to the total spin number $\{S^z_{\text{tot}}\} = \{S^z_{i,j+1} + S^z_{i,j} + S^z_{i+1,j}\}$ (i.e., $S^z_{\text{tot}} = \pm\frac{3}{2},\ \pm\frac{1}{2}$ if measured at zero field), we can recognize four isolated block Hamiltonians $\tilde{\mathcal{H}}_A^{\{S^z_{\text{tot}}\}}$ on the diagonal:

$$H^A_{i,j}(h) = \begin{pmatrix} (J_1+J_3-3h) & & & \\ & \begin{pmatrix} J_3-J_1-h & 2J_1 & 0 \\ 2J_1 & -J_1-J_3-h & 2J_3 \\ 0 & 2J_3 & J_1-J_3-h \end{pmatrix} & & \\ & & \begin{pmatrix} J_3-J_1+h & 2J_3 & 0 \\ 2J_3 & -J_1-J_3+h & 2J_1 \\ 0 & 2J_1 & J_1-J_3+h \end{pmatrix} & \\ & & & (J_1+J_3+3h) \end{pmatrix}$$

$$= \begin{pmatrix} \tilde{\mathcal{H}}_A^{\{-\frac{3}{2}\}}(h) & 0 & 0 & 0 \\ 0 & \tilde{\mathcal{H}}_A^{\{-\frac{1}{2}\}}(h) & 0 & 0 \\ 0 & 0 & \tilde{\mathcal{H}}_A^{\{+\frac{1}{2}\}}(h) & 0 \\ 0 & 0 & 0 & \tilde{\mathcal{H}}_A^{\{+\frac{3}{2}\}}(h) \end{pmatrix}.$$

For $H^B_{i,j}(h)$, we obtain another block-diagonal matrix $\tilde{\mathcal{H}}_B^{\{S^z_{\rm tot}\}}$:

$$H^B_{i,j}(h) = \begin{pmatrix} (J_1+J_3-3h) & & & \\ & \begin{pmatrix} J_3-J_1+h & 2J_3 & 0 \\ 2J_3 & -J_1-J_3+h & 2J_1 \\ 0 & 2J_1 & J_1-J_3+h \end{pmatrix} & & \\ & & \begin{pmatrix} J_3-J_1-h & 2J_1 & 0 \\ 2J_1 & -J_1-J_3-h & 2J_3 \\ 0 & 2J_3 & J_1-J_3-h \end{pmatrix} & \\ & & & (J_1+J_3+3h) \end{pmatrix}$$

$$= \begin{pmatrix} \tilde{\mathcal{H}}_B^{\{-\frac{3}{2}\}}(h) & 0 & 0 & 0 \\ 0 & \tilde{\mathcal{H}}_B^{\{-\frac{1}{2}\}}(h) & 0 & 0 \\ 0 & 0 & \tilde{\mathcal{H}}_B^{\{+\frac{1}{2}\}}(h) & 0 \\ 0 & 0 & 0 & \tilde{\mathcal{H}}_B^{\{+\frac{3}{2}\}}(h) \end{pmatrix}$$

$$= \begin{pmatrix} \tilde{\mathcal{H}}_B^{\{+\frac{3}{2}\}}(-h) & 0 & 0 & 0 \\ 0 & \tilde{\mathcal{H}}_B^{\{+\frac{1}{2}\}}(-h) & 0 & 0 \\ 0 & 0 & \tilde{\mathcal{H}}_B^{\{-\frac{1}{2}\}}(-h) & 0 \\ 0 & 0 & 0 & \tilde{\mathcal{H}}_B^{\{-\frac{3}{2}\}}(-h) \end{pmatrix} \equiv H^A_{i,j}(-h).$$

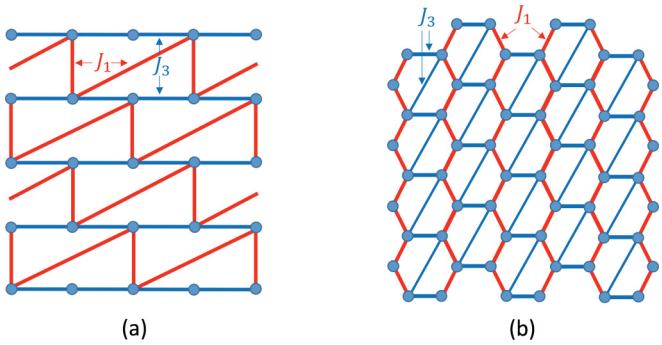

FIG. 18. (a) The rectangular lattice and (b) the topologically equivalent honeycomb lattice with additional interactions.

Thus, the two local Hamiltonians satisfy the condition of the equality provided that

$$H^A_{i,j}(h) \equiv H^B_{i,j}(-h). \tag{A7}$$

This condition states that the equivalency between the zigzag square lattice and the rectangular lattice is completely satisfied for the ground-state as well as finite-temperature properties such as energy, magnetization, specific heat, and susceptibility. The equivalence of the local Hamiltonians (A7) leads to the topological equivalence of all 2D lattices with the coordination number 4 with the constraint that two nearest neighbors are coupled by the interaction J and the other two nearest neighbors are coupled via RJ interaction (R varies between 0 and 1). Examples of such lattices are already given in Figs. 2(b)–2(e). Apparently, there exist other possibilities of how to modify the geometry of the three-spin blocks in Fig. 16 described by the local Hamiltonians (A4) and (A5)) by changing the angle at the middle spin or the bond length as in Figs. 2(b) and 2(d). In this respect, some other lattices (Fig. 18) can be constructed as a rectangular lattice with one interaction along a diagonal of the rectangular plaquette while the neighboring plaquette is shifted by half of the bond length. Another example is a honeycomb lattice with one interaction along a diagonal within the hexagon and others. All the aforementioned lattices look differently, but they topologically represent the identical system.

[1] U. Schollwöck, J. Richter, D. J. J. Farnell, and R. F. Bishop, *Quantum Magnetism* (Springer, Berlin, 2004).
[2] A. Orendáčová, R. Tarasenko, V. Tkáč, E. Čižmár, M. Orendáč, and A. Feher, Crystals **9**, 6 (2019).
[3] B. C. Keith, C. P. Landee, T. Valleau, M. M. Turnbull, and N. Harrison, Phys. Rev. B **84**, 104442 (2011); **84**, 229901(E) (2011).
[4] L. Siurakshina, D. Ihle, and R. Hayn, Phys. Rev. B **61**, 14601 (2000).
[5] C. Yasuda, S. Todo, K. Hukushima, F. Alet, M. Keller, M. Troyer, and H. Takayama, Phys. Rev. Lett. **94**, 217201 (2005).
[6] P. Sengupta, A. W. Sandvik, and R. R. P. Singh, Phys. Rev. B **68**, 094423 (2003).
[7] A. Orendáčová, E. Čižmár, L. Sedláková, J. Hanko, M. Kajňaková, M. Orendáč, A. Feher, J. S. Xia, L. Yin, D. M. Pajerowski, M. W. Meisel, V. Zeleňák, S. Zvyagin, and J. Wosnitza, Phys. Rev. B **80**, 144418 (2009).

[8] Y. Kohama, M. Jaime, O. E. Ayala-Valenzuela, R. D. McDonald, E. D. Mun, J. F. Corbey, and J. L. Manson, Phys. Rev. B **84**, 184402 (2011).

[9] G. Giuseppetti and F. Mazzi, Rend. Soc. Mineral. Ital. **11**, 202 (1955).

[10] D. Harvey and C. J. L. Lock, Acta Crystallogr. C **42**, 799 (1986).

[11] P. Sarmah, S. Singha, R. Chakrabarty, S. J. Bora, and B. K. Das, Indian J. Chem. A **46**, 1929 (2007).

[12] R. Kumar, S. Obrai, V. K. Joshi, V. Kumar, and S. Shahab, Commun. Inorg. Synth. **3**, 9 (2015).

[13] C. W. Chan, J. W. Lai, I. H. Ooi, H. M. Er, S. M. Chye, K. W. Tan, S. W. Ng, M. J. Maah, and C. H. Ng, Inorg. Chim. Acta **450**, 202 (2016).

[14] V. Zeleňák, A. Orendáčová, I. Císařová, J. Černák, O. V. Kravchyna, J.-H. Park, M. Orendáč, A. G. Anders, A. Feher, and M. W. Meisel, Inorganic Chemistry **45**, 1774 (2006).

[15] R. Rajan, Physica **29**, 1191 (1963).

[16] D. E. Billing, R. Dudley, B. J. Hathaway, P. Nicholis, and I. M. Procter, J. Chem. Soc. A **1969**, 312 (1969).

[17] R. Tarasenko, L. Lederová, A. Orendáčová, M. Orendáč, and A. Feher, Acta Phys. Pol. A **133**, 420 (2018).

[18] M. Zabel, V. I. Pawlowski, and A. L. Poznyak, J. Structural Chemistry **47**, 585 (2006).

[19] L. J. de Jongh and A. R. Miedema, Adv. Phys. **23**, 1 (1974).

[20] J. C. Bonner and M. E. Fisher, Phys. Rev. **135**, A640 (1964).

[21] A. Klümper, Eur. Phys. J. B **5**, 677 (1998).

[22] A. Klümper and D. C. Johnston, Phys. Rev. Lett. **84**, 4701 (2000).

[23] A. Cuccoli, T. Roscilde, R. Vaia, and P. Verrucchi, Phys. Rev. B **68**, 060402(R) (2003).

[24] Y. J. Kim and R. J. Birgeneau, Phys. Rev. B **62**, 6378 (2000).

[25] C. P. Landee (private communication).

[26] R. Nath, M. Padmanabhan, S. Baby, A. Thirumurugan, D. Ehlers, M. Hemmida, H.-A. Krug von Nidda, and A. A. Tsirlin, Phys. Rev. B **91**, 054409 (2015).

[27] L. Lederová, A. Orendáčová, J. Chovan, J. Strečka, T. Verkholyak, R. Tarasenko, D. Legut, R. Sýkora, E. Čižmár, V. Tkáč, M. Orendáč, and A. Feher, Phys. Rev. B **95**, 054436 (2017).

[28] H. Yamaguchi, Y. Tamekuni, Y. Iwasaki, R. Otsuka, Y. Hosokoshi, T. Kida, and M. Hagiwara, Phys. Rev. B **95**, 235135 (2017).

[29] A. W. Sandvik, Phys. Rev. B **59**, R14157(R) (1999).

[30] B. Bauer, L. D. Carr, H. G. Evertz, A. Feiguin, J. Freire, S. Fuchs, L. Gamper, J. Gukelberger, E. Gull, S. Guertler, A. Hehn, R. Igarashi, S. V. Isakov, D. Koop, P. N. Ma, P. Mates, H. Matsuo, O. Parcollet, G. Pawłowski, J. D. Picon, L. Pollet, E. Santos, V. W. Scarola, U. Schollwöck, C. Silva, B. Surer, S. Todo, S.Trebst, M. Troyer, M. L.Wall, P. Werner, and S.Wessel, J. Stat. Mech. (2011) P05001.

[31] A. H. C. Neto and D. Hone, Phys. Rev. Lett. **76**, 2165 (1996).

[32] A. L. Chernyshev and M. E. Zhitomirsky, Phys. Rev. B **79**, 174402 (2009).

[33] A. Lüscher and A. M. Läuchli, Phys. Rev. B **79**, 195102 (2009).

[34] J. M. Ziman, *Electrons and Phonons* (Oxford University, London, 1960).

[35] P. Sengupta, C. D. Batista, R. D. McDonald, S. Cox, J. Singleton, L. Huang, T. P. Papageorgiou, O. Ignatchik, T. Herrmannsdörfer, J. L. Manson, J. A. Schlueter, K. A. Funk, and J. Wosnitza, Phys. Rev. B **79**, 060409(R) (2009).

[36] S. Chakravarty, B. I. Halperin, and D. R. Nelson, Phys. Rev. Lett. **60**, 1057 (1988).

[37] T. Radu, H. Wilhelm, V. Yushankhai, D. Kovrizhin, R. Coldea, Z. Tylczynski, T. Lühmann, and F. Steglich, Phys. Rev. Lett. **95**, 127202 (2005).

[38] B. Bernu and G. Misguich, Phys. Rev. B **63**, 134409 (2001).

[39] L. Spanu and A. Parola, Phys. Rev. B **72**, 174418 (2005).

[40] R. Coldea, D. A. Tennant, K. Habicht, P. Smeibidl, C. Wolters, and Z. Tylczynski, Phys. Rev. Lett. **88**, 137203 (2002).

[41] M. E. Zhitomirsky and A. L. Chernyshev, Phys. Rev. Lett. **82**, 4536 (1999).

[42] M. Mourigal, M. E. Zhitomirsky, and A. L. Chernyshev, Phys. Rev. B **82**, 144402 (2010).

[43] K. Yu. Povarov, A. I. Smirnov, and C. P. Landee, Phys. Rev. B **87**, 214402 (2013).

[44] V. Kiryukhin, Y. J. Kim, K. J. Thomas, F. C. Chou, R. W. Erwin, Q. Huang, M. A. Kastner, and R. J. Birgeneau, Phys. Rev. B **63**, 144418 (2001).

[45] K. W. Blazey, H. Rohrer, and R. Webster, Phys. Rev. B **4**, 2287 (1971).

[46] A. Cuccoli, T. Roscilde, V. Tognetti, R. Vaia, and P. Verrucchi, Phys. Rev. B **67**, 104414 (2003).